1-1-2011

Development of signal processing for the broadband near infrared spectroscopy

Irina Schelkanova
Ryerson University

Development of Signal Processing for the Broadband Near Infrared Spectroscopy

by

Irina Schelkanova

Bachelor of Science, University of Toronto, 2008

A thesis

presented to Ryerson University

in partial fulfillment of the

requirements for the degree of

Master of Science

in the Program of

Biomedical Physics

Toronto, Ontario, Canada, 2011

I hereby declare that I am the sole author of this thesis.

I authorize Ryerson University to lend this thesis to other institutions or individuals for the purpose of scholarly research.

I further authorize Ryerson University to reproduce this thesis by photocopying or by other means, in total or in part, at the request of other institutions or individuals for the purpose of scholarly research.

Development of Signal Processing for the Broadband Near Infrared Spectroscopy

Master of Science 2011

Irina Schelkanova

Biomedical Physics

Ryerson University

Abstract

Near Infrared Spectroscopy (NIRS) uses optical radiation of the waveband between approximately 700 and 1000 nm to measure concentrations of light absorbing chromophores, such as, oxy-haemoglobin (HbO_2) and deoxy-haemoglobin (Hb).The objective of this thesis was to investigate and further develop the capabilities of broadband CW near infrared spectroscopy by capitalizing on the continuity of the optical properties of tissue as functions of the NIR wavelength. The thesis consists of four parts. The Introduction section covers relevant aspects of theory and mathematical concepts. Journal Manuscript part contains two projects: one is the research paper on the optimal algorithm of quantitation of the cerebral haemodynamic response in fNIRS. The second research article is on independent component analysis of functional near infrared spectroscopy data. For the first time, broadband NIR data were analyzed using individual wavelengths as the different input channels to separate the data into temporal independent components. The fourth part is allocated for the overall conclusion of the entire thesis.

Acknowledgements

This project has been accomplished with great assistance and source of strength from my family and friends. I deeply appreciate all the technical support and kind words of encouragement that I have received along the way towards my Masters. A special thank you to my supervisor, Dr. Toronov, whose dedication and professional guidance helped my transition and development into the field of biomedical physics. Many thanks also to both members of my supervisory committee, Dr. Adrian Crawley and Dr. Yuan Xu, for providing invaluable input to my research progress. It has been a pleasure working with them.

Also, I would like to acknowledge professional support from Administration of Ryerson University. A lot of resources was invested into me and my project. This research has been supported by the Ryerson University Faculty of Engineering, Architecture and Science Deans Research Fund.

Dedication

To all wonderful women of my family who supported and inspired me.

Contents

List of Tables

List of Figures

Research Objectives

The procedure of quantitation of blood chromophore concentrations by means of near infrared light is called Near Infrared Spectroscopy. Near infrared spectroscopy (NIRS) utilizes electromagnetic waves in the range of 650 to 1000nm to monitor physiological changes in the state of biological tissues. The optical properties of tissue chromophores within this range makes NIR especially suitable for clinical application as a standalone or in conjunction with other imaging modalities. The NIR research of monitoring of brain activity is motivated by its high potential. It is easier to manage and less costly alternative to imaging modalities such as functional magnetic resonance imaging (fMRI) and positron emission tomography (PET). Moreover, in addition to high biochemical specificity, the NIR method provides information about physiological parameters not available to other modalities, such as oxygenation information. Also, NIRS has higher temporal resolution, in the order of milliseconds, compared to fMRI and PET [1]. This allows measuring fast oscillatory physiological functions [2]. Furthermore, NIR equipment is relatively less restraining compared to fMRI or PET and generally safer than PET as it does not rely on ionizing radiation. Some types of NIR equipment, usually for continuous wave (CW) signals, have advantage of being portable, and even telemetric [3], [4], [5]. Lastly, real time measurements without removing subjects from their in-patient units, therefore not interfering with intensive care, as it is practiced in clinical neonatology is one of the promising areas of NRIS research [6]. Given these assets, the research into NIR based brain assessment have been growing via studies on brain dysfunction [7], education and training [8], and cognitive work load assessment [9].

The goal of these studies was to extend the capabilities of broadband CW near infrared spectroscopy by capitalizing on the continuity of the optical properties of tissue as functions of the NIR wavelength. The investigation included two parts: first, theory of light propagation in tissue applied to in-vivo broadband NIR data was used to quantify cerebral haemodynamic changes by employing four different mathematical formulations;

Second, in order to investigate whether ICA applied to the broadband NIR data can be used as an efficient tool of functional data analysis, a separation of the optical data into statistically independent temporal components was performed using FastICA and the spectrosocopic analysis of the independent components was performed.

Since in both studies one of the goals was to remove physiological noise from functional cerebral signals, fMRI was used as a gold standard measure of the deoxyhemoglobin concentration changes.

My hypotheses were that:

1) the time courses of oxy-haemoglobin and deoxy-haemoglobin concentrations can be more accurately recovered based on the continuity of the optical properties as functions of the wavelength than using isolated wavelengths of light.

2) correlation of cerebral hemodynamic signals acquired during breath hold task was improved when the $\Delta_{oxyHb}(t)$ and $\Delta_{deoxyHb}(t)$ changes are obtained using spectral derivative algorithms

3) ICA can recover mixed temporal components which would contain additional information about dynamic changes of the NIR chromophore concentrations.

The method consisted of several steps outlined in the Figure 1.1.

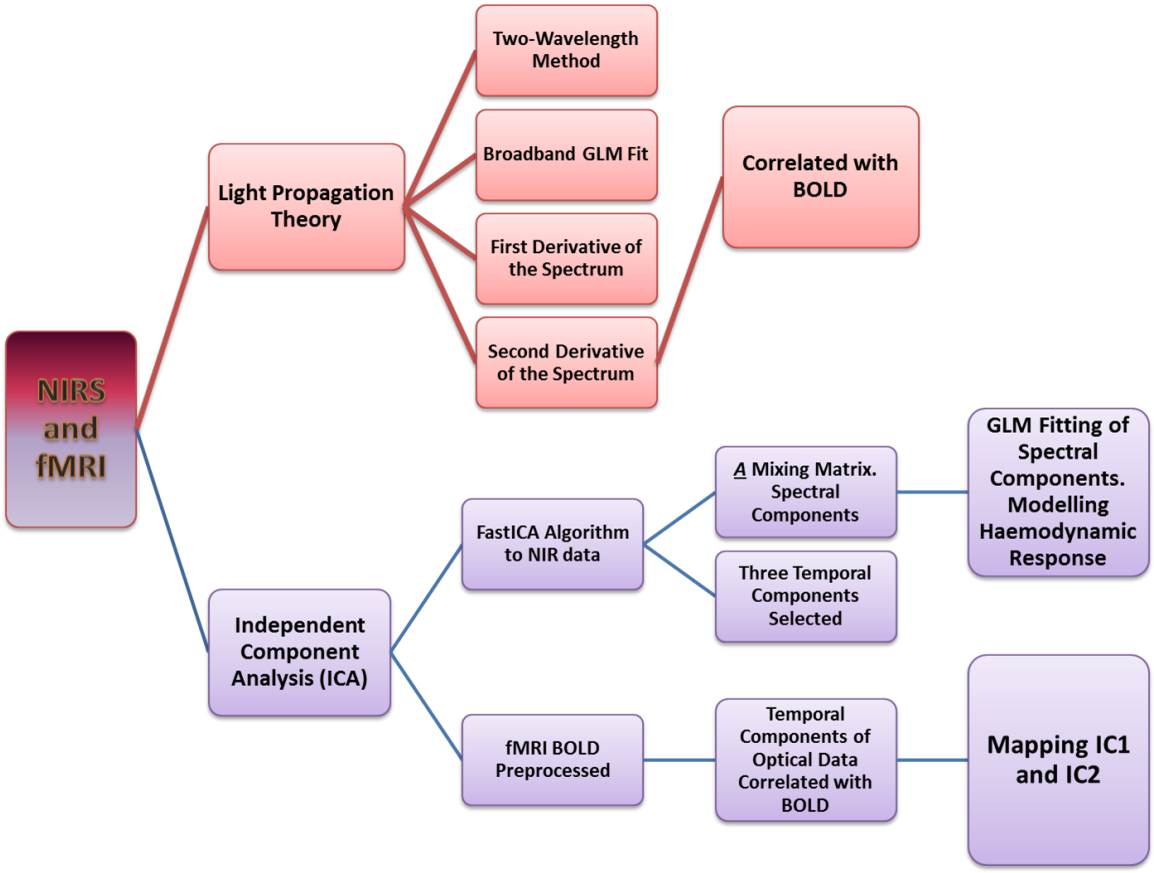

Figure 1: Schematic diagram of thesis organization

First, haemodynamic theory approach was implemented to the optical data collected simultaneously with BOLD fMRI. The second, FastICA statistical method was used to separate temporal components. Identified temporal components were correlated at each voxel with BOLD MRI signal. Spatial mapping of the temporal components based on the correlation coefficients were coded in colours. Further, several linear models were fitted into spectral components of the optical data. Statistical significance of the models was assessed.

Chapter 1

Introduction

1.1 NIR Imaging and Spectroscopy Systems

Three types of NIR imaging and spectroscopy systems have been in development for use in research on brain [3], [10]. The simplest of these three is a continuous wave (CW) system CW-type instruments are able to assess regional cerebral blood flow by measuring light attenuation through the cortical tissue and calculating their hemodynamic responses, i.e. changes in hemoglobin concentration and oxygenation, using the attenuated signal [11]. However, with this type of measurements, it is impossible to gauge the absolute concentration changes since the real path length of travelled light is unknown and cannot be measured or guessed. Therefore, CW-type instruments rely on simplified assumptions about the nature of the media being probed and the changes occurring inside the sampling volume. Only relative concentration changes from some baseline measurement can be assessed. The advantage of using a CW-type instrument is that they are inexpensive, and portable. An example of CW-type system used in our lab is pictured in Figure 1.2. As can be seen from the figure the entire system is quite compact. The probe itself is flexible, thus relatively comfortable to wear and consists of a semicircular array of light sources and a USB spectrometer.

In order to quantify absolute values of chromophore concentrations, the absorptive and scattering components of the light attenuation should be separated. This may be achieved with the aid of time-resolved or frequency domain methods. Time-resolved spectroscopy (TRS) was first pioneered by Delpy et. al. [12], Patterson et. al. [13] and Chance et al. [14], [15].TRS instruments use a picosecond pulsed laser and time-correlated photon counting detectors designed to measure the time evolution of the light intensity [4].Using the time profile of light intensity, it is possible to recover both absorption and scattering coefficients of the probed media [16]. A major drawback of TRS instruments is that they are expensive and not quite portable.

Frequency domain method was first suggested by Gratton et. al. in [17]. Frequency domain approach uses radio frequency intensity modulated sources (100 MHz and higher). In addition to the DC component of the optical signal frequency domain systems can measure phase and modulation amplitude which

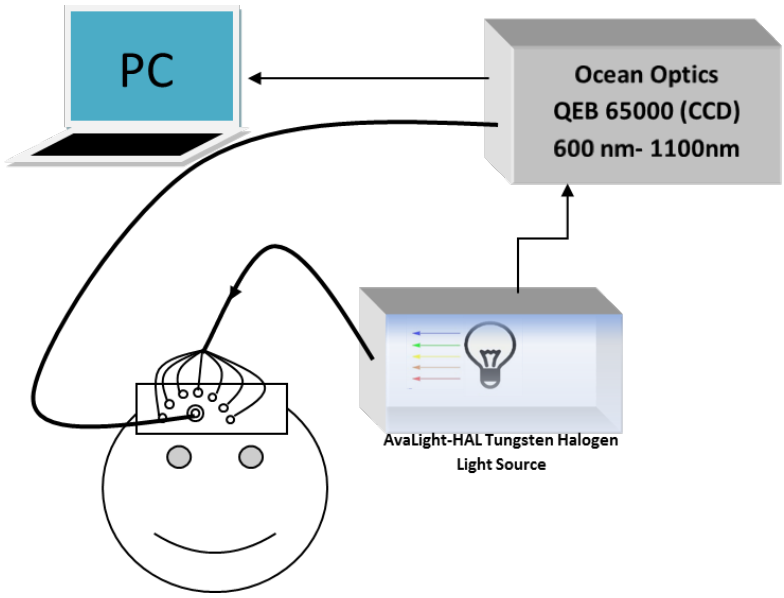

Figure 1.1: An example of CW-type system: 1. PC Station for recording data; 2. CCD Spectrometer (QE 65 000); 3. White light source; 4. Probe attached to the forehead of a volunteer.

can all be related back to the absorptive and scattering properties of the medium. Frequency domain method is mathematically related to TRS via Fourier transform [18]. However, frequency domain systems have an advantage of being a relatively inexpensive alternative to TRS systems. The disadvantage of frequency domain systems is that they can only provide information at a finite number of modulation frequencies.

1.2 Near Infrared Light in Tissue

F. F. Jobsis pioneered work in NIRS and demonstrated that the state of cortical tissue can be monitored noninvasively [19] by shining near infrared light through the skull. Some of the first demonstrations of brain activity monitoring were performed by Chance et. al. [14], Cope, Villringer et. al. [20]. Light is absorbed differently by various layers of the head such as skin, skull and brain. Some part of the input light exits the head after following the so-called "banana" pattern due to scattering effect of the tissue (Figure 1.3). This backscattered photons, detected at various distances from the source, carry information about functional state of the brain.

When the absorption spectrum of light is analyzed, it is seen that the main signal comes from blood chromophores such as oxygenated and deoxygenated haemoglobin (HbO_2 and Hb, respectively), water, and, possibly, cytochrome [21]. Lipid is considered to be relatively transparent to NIR light. Therefore, changes in the amplitude of backscattered light can be interpreted as changes in blood chromophore concentrations. Blood chromophore information can be used to estimate cerebral blood volume (CBV)

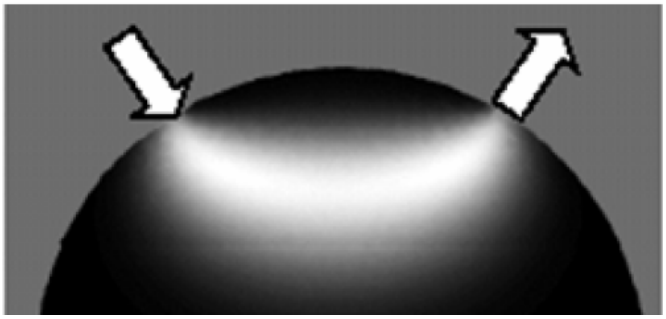

Figure 1.2: The banana-shaped light path through a tissue sample. From [18]

and tissue oxygen saturation, which are indications of haemodynamic activity [18]. Physiology of this response can be described mathematically by means of haemodynamic theory.

When near infrared light is shone into the tissue, injected photons follow various paths inside the head. It is due to the fact that biological tissue is a highly scattering heterogeneous medium comprised of many scatterers of various sizes and indices of refraction, causing the electromagnetic wave to refract at each interface at many different angles [12]. The scattering property of tissue is wavelengths dependent. It is represented by the scattering coefficient ($\mu_s(mm^-1)$), and thought of as a probability of a photon scattering per unit length [22]. The inverse of scattering coefficient is termed as the mean free path of photons, and it is measured in units of lengths. Besides the size of the scaterers, the angle of reflection is dependent on the wavelength of the source, and the initial direction of the injected ray [23]. This parameter is called the anisotropy factor of scattering, g.

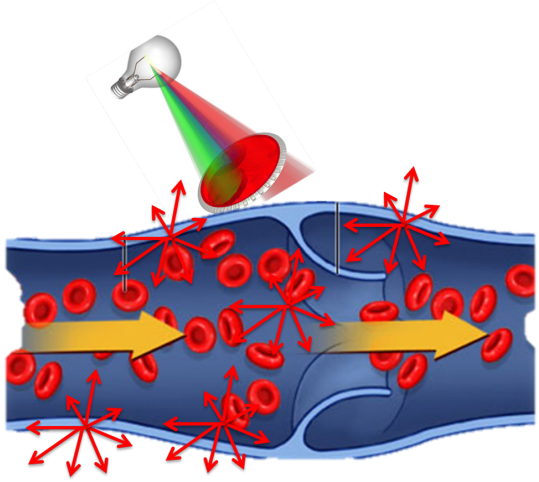

Figure 1.3: Propagation of electromagnetic wave in biological tissue. When light rays enter biological tissue, they divide into infinitely many new beams due to the scattering. When electromagnetic waves are scattered it changes the direction of propagation of the wave. From Healthwise, Inc.

Another wavelength dependent property of a living tissue is absorption [20]. Absorption coefficient ($\mu_a(mm^-1)$) is defined as the linear attenuation rate of irradiance per unit of length [22]. Tissues can be differentiated by the way they interact with light according to their specific absorption, scattering and anisotropic properties [12].

Modelling light transport in tissue allows quantitation of optical measurements. The fundamental equation which describes propagation of light in highly scattering media is the radiative transfer equation (RTE) [24]. The number of photons per unit volume, $\phi(r, \hat{s}, t)$ travelling from point r in direction $\hat{s}$ at time t is equal to the sum of all the mechanisms which increase it minus those effects which reduce it [24].

$$\left(\frac{1}{c}\frac{\partial}{\partial t} + \hat{s}.\nabla + \mu_a(r) + \mu_s(r)\right)\phi(r, \hat{s}, t) = \mu_s(r)\int_{s^{n-1}} \Theta(\hat{s}, \hat{s'})\phi(r, \hat{s}, t)d\hat{s'} + q(r, \hat{s}, t) \tag{1.1}$$

In (1.1), $\Theta(\hat{s}, \hat{s'})$ is the scatter phase function, which gives the probability of a photon scattering from direction $\hat{s}$ to $\hat{s'}$, and $q(r, \hat{s}, t)$ is the light source at r at time t travelling in direction $\hat{s}$ [24].

For modelling propagation of light through the turbid media, the diffusion approximation to the radiative transfer equation is acceptable because the source-detector separation distances are much greater than the mean free path of light particles [12]. This approximation is based on the assumption that all the particles will be scattered isotropically, and therefore, all the energy will be distributed equally [25]. This means that every time a wave changes its direction of propagation due to scattering, it may take off in a new direction with a uniform probability. The diffusion approximation of the transport equation is represented by the diffusion equation [26]:

$$c\mu_a U(r,t) + \frac{\partial U(r,t)}{\partial t} - cD\Delta U(r,t) = Q(r,t) \tag{1.2}$$

where $U(r,t)$ represents the photon density, i.e. the volume energy of light, in units of J/cm^3, $D = (3\mu_a + 3\mu_{s'})^{-1}$ is the diffusion coefficient in units of cm^2/s and $\mu_{s'}$ represents the reduced scattering coefficient $\mu_{s'} = \mu_s(1-g)$. The purpose of $\mu_{s'}$, is to describe the diffusion of electromagnetic waves as a series of random step sizes of $1/\mu_{s'}(cm)$, where each step involves isotropic scattering [22]. $Q(r,t)$ is the source term. The main assumption of the diffusion approximation is that the scattering is dominant over the absorption, i.e. $\mu_{s'} \gg \mu_a$ [27]. This condition is generally true for tissue types such as skin and cerebral matter, and not true for tissue for which this approximation does not hold such as cerebrospinal fluid, eye lenses and nails. Hence, the diffusion approximation can be employed in many biomedical applications at NIR wavelengths [27].

1.2.1 Haemodynamic Response and Modified Beer-Lambert Law (MBLL)

The most widely used model of calculating haemodynamic response to stimuli is based on the Beer-Lambert law [28]. It describes a linear relationship between absorbance, A, of light in a medium and

the concentration of the chromophore, C. This relationship is given by Equation (1.3)

$$A = log\frac{I}{I_0} = \epsilon(\lambda)CL \tag{1.3}$$

where $I = I_0 exp\epsilon(\lambda)CL$ is the spectral fluence of the transmitted light,I_0 is the fluence of the incident light, C is the concentration of the chromophore and L is the path length. Delpy et. al. were the first to introduce the modified Beer-Lambert law [12], [29], [30]. Modified Beer-Lambert law (MBLL) relies on the assumption that the medium is homogeneous and has the property of constant scattering [31].

For non-scattering media, following the classical Beer-Lambert law, L is equal to the distance between source and detector, denoted as d. For scattering media Equation (1.3) can be rewritten as

$$A = \epsilon(\lambda)C \cdot d \cdot DPF(\lambda) + G(\lambda) = \epsilon(\lambda)C \cdot < L > + G(\lambda) \tag{1.4}$$

where G is the contribution of the attenuated light due to scattering and $DPF =< L > /d$ is called the differential path length factor, and $< L >$ is the mean path length of the detected photons [28]. The differential path length factor describes the increase in path length due to tissue scattering. If the value of wavelength dependent G is not known, it is not possible to assess the absolute value of A, but DPF and G can be assumed to be constant. This allows for assessment of changes in chromophore concentration. This is generally considered a plausible assumption when measuring hemodynamics, since changes in oxygenation and concentration of hemoglobin affect the absorption coefficient more significantly than the scattering coefficient [31]. The Equation (1.4) can then be rewritten as

$$\Delta A = A_t - A_{t0} = \epsilon(\lambda) \cdot \Delta C \cdot d \cdot DPF(\lambda) \tag{1.5}$$

where A_t is the absorbance at some time t after the change in concentration of chromophores and A_{t0} is the initial absorbance. Each chromophore has specific extinction spectrum in the near-infrared range, which allows for measurements of concentration changes in several chromophores simultaneously by taking optical measurements at multiple wavelengths (broadband spectroscopy). The main chromophores in the optical window of 600 to 900nm, are oxy- and deoxy-haemoglobin (HbO_2 and HB respectively), water, lipids, and cytochrome-c-oxidase (Figure 1.5).

These are the main chromophores of interest in NIR spectroscopy of the brain because during stimulations the greatest absolute changes occur in the concentrations of HbO_2 and Hb. [10], [32]. Some studies also report changes in cytochrome-oxidase redox, however, many researchers question the detectability of changes in cytochrome-oxidase redox [33], [34], [32]. Uludag et. al. argued that concurrent detection of changes in cytochrome-oxidase redox state with those of hemoglobin concentration and oxidation might be severely affected by the cross-talk error where the magnitude of the error for the redox state of cytochrome-c-oxidase may be in the order of those detected experimentally [35].

Oxy- and deoxy-haemoglobin concentrations are of particular interest because they are related to the regional cerebral blood flow (rCBF). A focal change in rCBF indicates an activation state [31]. Using N wavelengths of light one can solve N simultaneous linear equations for each of the N chromophore concentration changes, in particular assuming changes in chromophore concentrations other than HbO_2

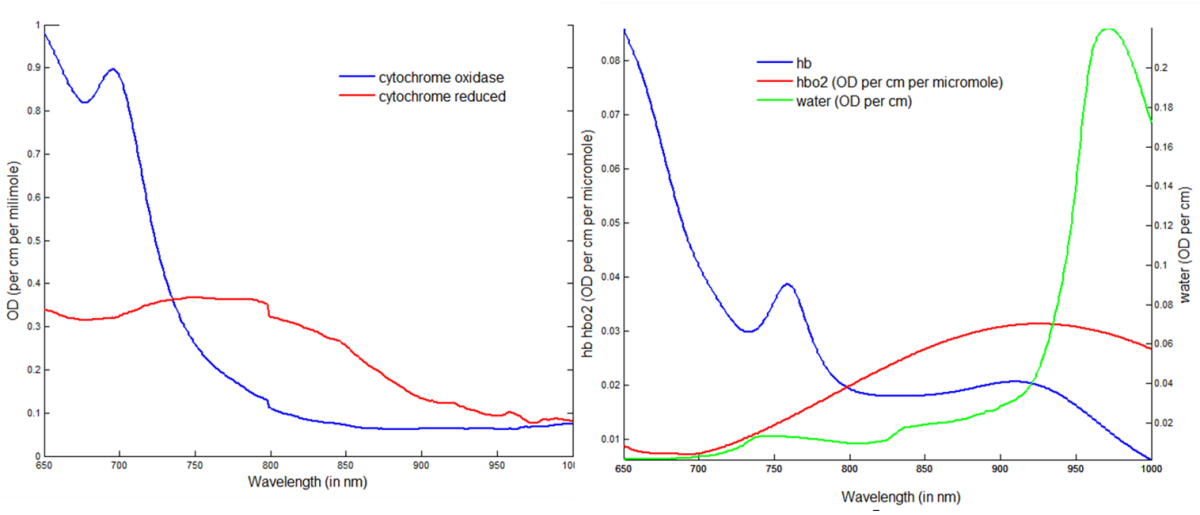

Figure 1.4: Graphs of the absorption spectra for HbO_2, Hb (optical density (OD) per cm per micromole), water (OD per cm), cytochrome-c-oxidase, and reduced cytochrome-c-oxidase (OD per cm per millimole).

and Hb small. To separate the contributions from HbO_2 and Hb, Equation (1.5) can be expressed as

$$\Delta A(\lambda) = (\epsilon_{HbO_2}(\lambda)\Delta[HbO_2]) + \epsilon_{Hb}(\lambda)\Delta[Hb]) \cdot DPF(\lambda) \cdot d \tag{1.6}$$

where $\Delta[HbO_2]$ is the change in HbO_2 concentration and $\Delta[Hb]$ is the change in Hb concentration. Given Equation (1.6), and assuming that the extinction spectra for each chromophores $\epsilon(\lambda)$ are known, concentration changes can be obtained by solving the two simultaneous equations at two distinct wavelengths. The generalization to more than two wavelength is discussed in [36].

However, the simplifying assumptions of homogeneous medium and homogeneous change in partial volume are inadequate for most biological media. The banana shape of the volume of interrogation [37], [38], Figure 1.3, is inaccurate because it is affected by cerebrospinal fluid (CBF) [39] and the pial cerebral vessels on the surface of the brain [40]. This raises the question of the layered contribution to the path of light that is not accounted for under the MBLL assumptions. Under the assumptions of MBLL, magnitudes of concentration changes are underestimated because the activated volume might be smaller than the sampling volume, (the partial volume effect) [35].

Furthermore, the wavelength dependence of optical tissue properties means that this partial volume effect is wavelength dependent. The accuracy of the measured local haemodynamic change depends on the knowledge of the partial path length within the partial volume, which is unknown. As a result, change in one chromophore concentration may mimic the effect of another, giving rise to crosstalk errors [41]. In the MBLL model, wavelength dependence is ignored by using a constant mean path length independent of wavelength. Calculating the concentration changes of chromophores using measured absorbance changes at different wavelengths will give rise to distortions in the extinction spectra. Thus,

accounting for the effect of layers is necessary. There has been some progress in layered modeling based on continuous wave broadband methods [42].

1.2.2 Diffuse Optical Tomography

Instead of MBLL, a diffuse optical tomographic(DOT) method for photon propagation in the brain was suggested [10]. The DOT is based on the diffusion. The general form of the diffusion equation is [18]

$$D(r)\nabla^2\Phi(r,t) + \upsilon\mu_a\Phi(r,t) + \frac{\partial\Phi(r,t)}{\partial t} = \upsilon S(r,t) \tag{1.7}$$

where $\Phi(r,t)$ is the photon fluence at position r and time t, $S(r,t)$ is the source, $D = \upsilon/(3\mu_{s'})$ is the diffusion coefficient, $\mu_{s'}$ is the reduced scattering coefficient, $\mu_a = \epsilon(\lambda)\cdot C$ is the absorption coefficient and υ is the speed of light through the medium. Equation (1.7) accurately models photon propagation under the assumption that scattering dominates a medium. The goal in DOT is to reconstruct the 3-D distribution of absorption and scattering coefficients of the medium given boundary data. There are many analytical and numeric techniques to solve Equation (1.7) for different geometry of the medium and with various boundary conditions.

1.3 Neurovascular Coupling and Sources of Physiological Noise

Acknowledging the distinction between tissue oxygenation and blood oxygenation, it is necessary to understand what can be monitored by NIRS. Tissue oxygenation refers to the amount of oxygen stored directly in the tissue - this cannot be monitored by NIRS. Blood oxygenation refers to oxygen saturation of the blood (oxygen transport) - this can be monitored by NIRS. These are two competing mechanisms because their time courses overlap [43]. The mechanism of the hemodynamic response following a neural activation is: *a*) a fast early regional increase in $deoxyHb$ without a concomitant decrease in $oxyHb$; *b*) followed by a slow increase in oxyHb with a concomitant decrease in $deoxyHb$ due to increased CBF in a wider region of the brain; *c*) higher intensity of stimulation results in a bigger response [43].

Temporal NIR signals measured on a healthy adult human cortex are generally expected to contain four frequency bands centered around $0.8Hz$, $0.2Hz$, $0.1Hz$ and $0.03Hz$ [44]; [45]; [32]. A classic example of the power spectral density (PSD) of the post stimulus signal is shown in Figure 1.6. The haemodynamic response following neural activation is embedded in the $0.1Hz$ - $0.03Hz$ band. The $0.8Hz$ and $0.2Hz$ bands correspond to heart rate and respiration respectively [46]. The $0.03Hz$ band, known as $B-waves$, is assumed to reflect the periodic variations generated by the brains vasomotor tone mechanisms [47]. The $0.1Hz$ band ($V-signal$, Mayer waves or $M-waves$) has the greatest effect on event-related optical signal (EROS) [48]. Vasomotion, i.e. the rhythmic dilation and contraction of the precapillary sphincters in the cortical capillary beds is suspected to be the origin of the V signals. It is affected by hypercapnia and rate of respiration [32].

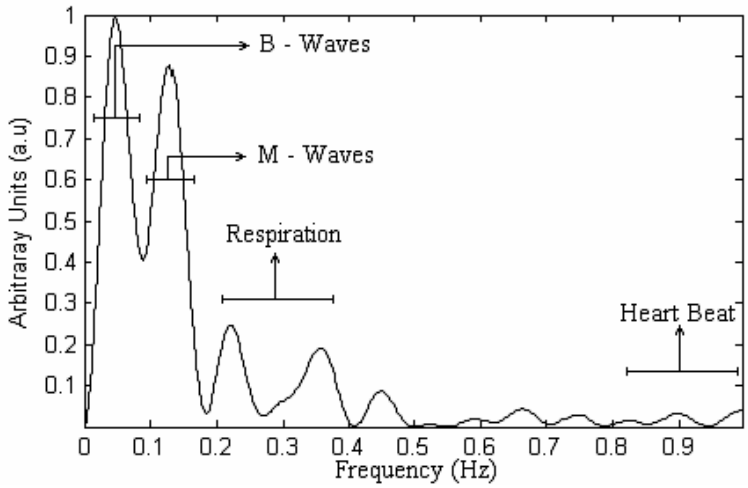

Figure 1.5: Spectral signature of the measured optical signal following a stimulus. From .

1.4 Physiological Interpretation of NIR and BOLD Signals

The haemodynamic response over an activated area of the brain can be described by a decrease in Hb along with a simultaneous increase in HbO_2 [31]. The amplitude of the increase in HbO_2 is approximately two to three times that of the decrease in Hb. Recording Hb response has an added benefit that it can be compared with fMRI blood oxygenation level dependent (BOLD) response as increase in the BOLD contrast is highly correlated with a decrease in Hb. Both NIR and fMRI have the same mechanism of activation.

A generalized model of NIR and BOLD signals can be conceptualized as follows: during functional stimulation, greater demand for oxygenation occurs, and the rate of oxygen consumption in a stimulated area increases. In response to this, the rate of cerebral blood flow (CBF) and cerebral blood volume (CBV) in the activated site increases due to vasodilation of previously constricted capillaries. As the local blood volume increases, the oxygen extraction rate drops due to the higher velocity of blood flow, leading to capillary and venous blood become more oxygenated (Figure 1.7).

1.5 Functional Magnetic Resonance Imaging

1.5.1 Physics and Physiology of the BOLD Contrast Mechanism

Functional Magnetic Resonance Imaging (fMRI) comprises a number of MRI techniques that investigate the functionality of cerebral activity. According to the properties to which the MRI signals are sensitive, these techniques can be generally categorized into susceptibility based, flow-based, or perfusion-based [49], [50], [51]. The most widely used is a susceptibility-based method fMRI study [52].

As normal brain energy production depends on oxidative metabolism, there is great local demand

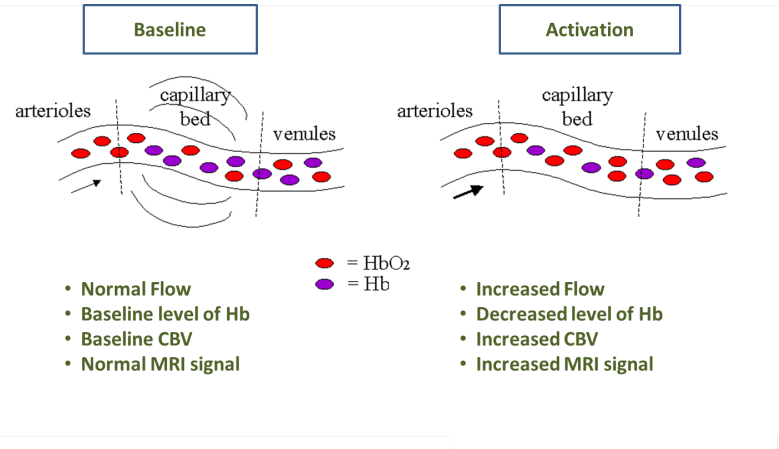

Figure 1.6: Illustration of mechanism of NIR and BOLD. From .

for delivery of oxygen with increased neuronal activity. To meet this increased metabolic consumption, neuronal activation is accompanied by increased local blood flow. This leads to an increase in the $oxy - Hb$ concentration, and a decrease in $deoxy - Hb$ concentration. Hemoglobin makes up nearly $15g$ per $100cm^3$ of normal blood [53]. The healthy red cell looks like a flattened disk, $\sim 6\mu m$ wide and $1 - 2\mu m$ thick, accounting for about 40% of the blood volume. The iron molecule in the heme group of deoxyhaemoglobin is paramagnetic, but the molecule becomes diamagnetic as oxyhemoglobin, heme with a bound oxygen molecule [54].

For the first time, Ogawa and Lee observed that blood vessel appeared darker, and the contrast of fMR images varied with blood-oxygen-level-dependence (BOLD) [55]. They attributed the signal increase to a magnetic susceptibility effect associated with the paramagnetic deoxyhaemoglobin in red cells because the magnetic susceptibility (χ) of more oxygenated blood is closer to that of the surrounding vascular tissue. This magnetic susceptibility associated with the oxygenation level and volume of cerebral blood shortens value of $T2^*$, providing the endogenous contrast agent for imaging in the brain [56], [57]. Typical values of the dimensionless χ for water -9.0, soft tissue -9.5, bone -9.0, fat -7.5, and air $+0.4$ (in parts per million under the SI unit system) [58]. Echo-planar imaging (EPI) is a frequent choice for BOLD fMRI studies due to its short acquisition time and its inherent sensitivity to magnetic susceptibility as compared to a spin-echo sequence (Figure1.8) [55], [51], [59]. The time course of the human BOLD response to a brief stimulus, the temporal impulse response function, is often called the hemodynamic response function (HRF). There is heterogeneity in the HRF across cortex of an individual observer, between observers, and possibly across different sensory, motor, and cognitive tasks [60], [61], [62], [63].

Besides the above physiochemical and haemodynamic reasons, cerebral blood volume (CBV) and cerebral blood flow (CBF) also affect the BOLD signal because of their direct effects on the intensity of the MRI signal [64]. CBV refers to the fraction of tissue occupied by blood (typically 3%). CBF is defined as the volumetric flow rate of blood within a given amount of tissue, which has a unit of milliliter per gram per second. The effect of CBF on the MRI signal may be different depending on its velocity. At

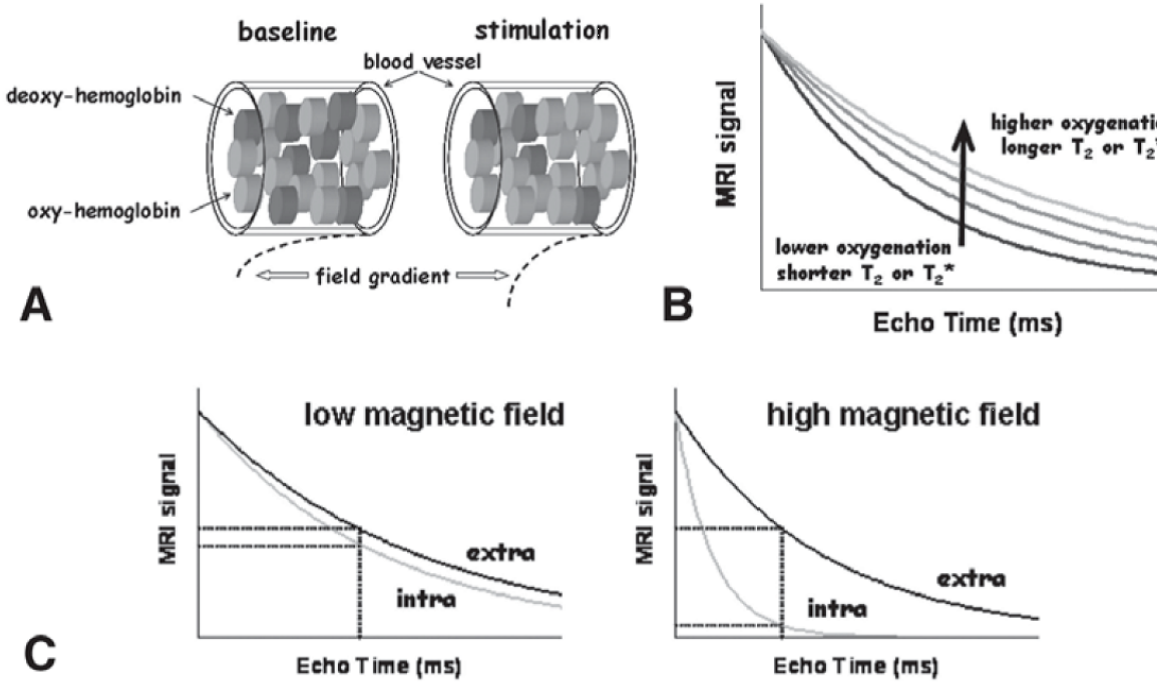

Figure 1.7: The biophysical basis of fMRI. (A) Because deoxyhaemoglobin is paramagnetic, the presence of this endogenous MRI contrast agent inside cerebral capillaries generates local magnetic field gradients that extend into cerebral tissue. The local gradients enhance dephasing of water protons in the tissue, which can be detected by decreased signals in $T2SE$ - and $T2GE$ - weighted images. (B) During activation, the amount of deoxyhaemoglobin is decreased in comparison with the resting condition; this difference between the stimulation-induced susceptibility difference of blood can be observed as changes in $T2^*$ by GE sequence. (C) At any given static magnetic field strength, the intravascular and extravascular weightings in BOLD data depend on the transverse relaxation times of water in blood ($T2$ intra; gray) and tissue ($T2$ extra; black). From [55].

low velocity, where the transient time of blood within a voxel is comparable to the repetition time (TR), CBF increase the MRI signal because the perfusion of fresh blood reduces the effective longitudinal relaxation time constant $T1$, which is also termed an inflow effect. On the other hand, at high velocity, where the transient time is comparable to TE/SE, CBF decreases the MRI signal because the exiting magnetized blood reduces the effective transverse relaxation time constant $T2^*$. For a BOLD fMRI study at $3T$, in a case where the voxel size is $5 \times 5 \times 5mm^3$, $TE = 25ms$, and $TR = 2000ms$, the velocity of blood flow is characterized as high for approximately $5mm/25ms = 200mm/s$, and low for about $5mm/2000ms = 2.5mm/s$ [64]. While such a high velocity only occurs in very large arteries, the low velocity is close to the typical flow rate inside the capillary bed. Therefore, in reality the inflow effect dominates. It should be noted that if TR is much longer than $T1$, approximately $800 - 1100ms$ for gray and white matter at $3T$, the inflow effect is negligible. Furthermore, blood flow results in phase shifts in

the MRI signal [59]. This will reduce the intensity of the MRI signal if the phase shift within a voxel is inhomogeneous. Knowing that the size of blood vessels ranges from millimeters (such as the network of veins on the surface of the brain) to micrometers (typical capillary size is $6 - 10\mu m$), it is almost certain that some voxels within the field-of-view (FOV) are highly inhomogeneous [64].

The involvement of multiple factors and uneven temporal behavior has greatly complicated the interpretation of the physiological mechanisms of BOLD signal. For example, the increment of cerebral metabolism rate of oxygen ($CMRO_2$) occurs almost instantly following the onset of the functional stimulation, which results in a change in the blood oxygenation level dictated by the dynamics of oxygen diffusion within plasma and across the blood-tissue barrier. In response to such a higher demand for oxygen, CBF rate increases [51]. This will in turn affect the CBV of tissue as well as the blood oxygenation level. The percentage of relative changes of CMRO2, CBF, and CBV are also different, and the typical range of the BOLD signal is only about $0.5 - 5.0\%$. Thus, it appears that it is difficult to study cerebral activity quantitatively using BOLD fMRI without a precise physiological model for the BOLD signal [60].

1.5.2 Brain Research Using BOLD fMRI

One of widely used activation paradigms in fMRI is the so-called block paradigm, which consists of alternated periods of activation (or task A) and rest (or task B). Each block is of equal duration, typically in the range $20 - 30s$. After an fMRI experiment has been designed and carried out, the resulting data must be passed through various analysis.

In a typical fMRI session a low-resolution functional volume is acquired every few seconds. Because the images are taken using an MR pulse sequence which is sensitive to changes in the local blood oxygenation level, parts of the images taken during stimulation should show increased intensity, compared with those taken during rest. The parts of these images which show increased intensity should correspond to the brain areas which are activated by the stimulation. The goal of fMRI analysis is to detect, in a robust, sensitive, and valid way, those parts of the brain which show increased intensity at the points in time that stimulation was applied. A single volume is made up of elements called voxels. An example time-series from a single voxel is shown in Figure 1.9.

1.5.3 Preparing fMRI Data for Statistical Analysis

Before conducting a statistical analysis, a $4D$ data set is pre-processed to maximize the signal-to-noise ratio (SNR). The signal-to-noise ratio is a measure of how big the signal of interest is, compared with the noise level. The signal of interest, in this case, is the change in image intensity which arises as a result of application of stimulation. A raw MR signal is obtained by digitizing the demodulated RF signal that is detected by the receiver coil [65]. The raw data that is thus generated does not resemble a real image, but instead is $k - space$ data, that is, a spatial frequency transformation of real-space. Additional reconstruction steps are also often necessary in order to correct for various artifacts in the data, or to otherwise improve the quality of the resulting image:

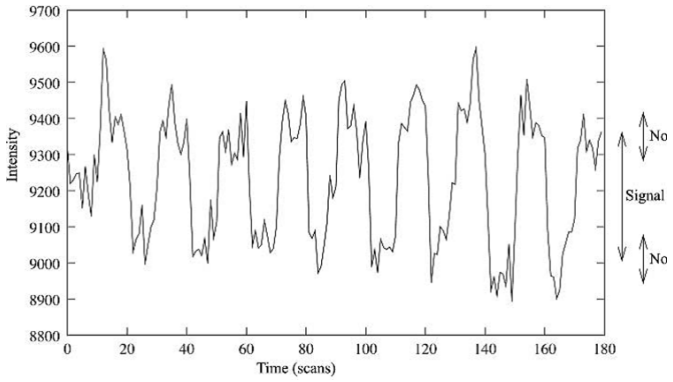

Figure 1.8: Image intensity versus time (in scans). The aim of fMRI analysis is to identify voxels in which the signal of interest is significantly greater than the noise.

Functional volumes are normally formed one slice at a time; the capture of these slices is spread out in time over the few seconds that the total volume capture takes. A problem with this is that later fMRI analysis assumes that all slices were captured at the same time. However, because different points in the volume were scanned at slightly different times, the model fitting is not optimal. The fitting will be improved if each voxels time series is adjusted so that it really does appear as if all voxels were scanned at the same time. This adjusting of time series is normally referred to as slice timing correction, and is achieved by phase shifting the time series of values at each voxel. Phase shifting means sliding the $1D$ time plot forwards or backwards; because the correction is small, a very small amount of sliding is required [65].

If a subject moves their head during an fMRI session, the position of the brain within the functional images will vary over time. This means that any particular voxels time series does not refer to the same point in the brain [65].

The next stage of fMRI analysis is the spatial filtering (blurring) of each volume. There are two reasons for applying spatial filtering as a pre-processing step; first, blurring can increase signal-to-noise ratio in the data, and second, certain later statistical steps, in order to be valid, may require the functional images to be spatially smooth [65]. The main point of spatial filtering of the fMRI data is to reduce the noise level whilst retaining the underlying signal. It is obvious why noise is reduced; the blurring function is effectively a local averaging, so the noise values in the local neighbourhood will tend to cancel each other out. In order for the underlying signal to not be reduced along with the noise, it is required that the extent of the blurring is not larger than the size of the activated region; if very small activation regions are expected then spatial filtering should not be carried out. The secondary reason for spatial filtering is that certain statistical theory which may be used in later processing requires the data to be spatially smooth for the assumptions underlying the statistical theory to be valid [66]. However, the amount of smoothing required for this is generally quite small (a $4mm$ width blurring function is generally adequate).

Temporal filtering, instead of working on each (spatial) volume separately works on each voxels time

series separately [65]. Because most basic statistical analyses also operate directly on voxel time series, it makes sense to carry out this step after all the previously described pre-processing stages, as each voxels time series should then be optimally conditioned. The main point of temporal filtering is to remove unwanted components of a time series, without, of course, damaging the signal of interest. Temporal filtering will normally attempt to remove components in the time series which are more slowly varying than this $60s$ periodic signal (high-pass filtering or drift removal) and also remove components which are more quickly varying (low-pass filtering, or noise reduction).

1.5.4 Statistical Analysis of Activation Images

Statistical analysis is concerned with making inference about underlying patterns in data that often contain a large amount of random error. This is certainly the case with fMRI data, where the effect of a stimulus may be as little as 1% of the BOLD signal [65]. After the pre-processing steps, statistical analysis is carried out to determine which voxels are activated by the stimulation. This can be simple correlation analysis or more advanced modelling of the expected hemodynamic response to the stimulation. The main output from this step is a statistical map which indicates those points in the image where the brain has activated in response to the stimulus.

It is most common to analyze each voxels time series independently, for example, univariate analysis such as standard general linear model (GLM) analysis [65]. However, there are also multivariate methods [67] which process all the data together. General linear modelling sets up a model and fits it to the data [68]. If the model is derived from the timing of the stimulation that was applied to the subject in the MRI scanner, then a good fit between the model and the data means that the data was probably caused by the stimulation.

An example of linear modelling is $y(t) = \beta^* x(t) + c + e(t)$, where $y(t)$ is the data, and is a $1D$ vector of intensity values, one for each time point, i.e. is a function of time [65]. $x(t)$ is the model, and is also a $1D$ vector with one value for each time point. In the case of a square-wave block design, $x(t)$ is a series of $1s$ and $0s$ - for example, 000001111100000 etc. β is the parameter estimate for $x(t)$, i.e. the value that the square wave (of height 1) must be multiplied by to fit the square wave component in the data. For fMRI experiments, the GLM is often formulated in matrix notation. Thus all of the parameters are grouped together into a vector $\boldsymbol{\beta}$, and all of the model time-courses are grouped together into a matrix $\boldsymbol{x}$, often referred to as the design matrix. c is a constant, and in this example, would correspond to the baseline (rest) intensity value in the data. e is the error in the model fitting.

Thus the model fitting involves adjusting the baseline level and the height of the square wave, to best fit the data; the error term accounts for the residual error between the fitted model and the data. In order to improve the fit of the model to the data, the stimulus function (which has a square waveform) is convolved with the hemodynamic response function [69]. This process mimics the effect that the brains neuro-physiology has on the input function (the stimulation) because the brains hemodynamic response is a delayed and blurred version of the input time-series.

When the model is fit separately to the data at each voxel, there will be found an estimate of the goodness of fit, of each column in the model, to that voxels time-course. To convert a parameter

estimate (PE, i.e. the estimated β value) into a statistics, its value is compared with the uncertainty in its estimation (resulting in a t value; $t = PE$ / standard error (PE)) [65]. If the PE is low relative to its estimated uncertainty, the fit is not significant and vice versa. Thus t is a good measure of whether the estimate of the PE value is significantly different from zero, i.e. whether there is believable activation. To convert a t value into a P (probability) or Z statistic requires standard statistical transformations; however, t, P, and Z all contain the same information - they describe how significantly the data is related to a particular part of the model [70]. The next step is to threshold this, in order to decide, at a given level of significance, which parts of the brain were activated.

The simplest method of thresholding is to select a significance (p) threshold and apply this to every voxel in the statistic map. A problem with this is that there are many tests being carried out, because there are so many voxels in the brain. If 20000 voxels are tested for at a significance of $p < 0.01$ then it is expected that 200 will activate by chance, even if no stimulation is applied. This multiple-comparison problem means that it is not valid to accept all activations reported by this method of thresholding; a correction is necessary to reduce the number of false positives [70]. Typically a Bonferroni correction is used, where the significance level at each voxel is divided by the number of voxels; this corrects for the number of comparisons being made. However, this results in very stringent thresholding (i.e. in the case given above, the resulting p threshold is $0.01/20000 = 0.0000005$). Thus instead of assigning a p - value to each voxel, clusters of voxels are created on the basis of an initial thresholding, and then each cluster is assigned a p - value, which may or may not pass the final significance test.

1.5.5 Multimodality Imaging with Optical Methods

NIRS has a number of important advantages for neurophysiological investigations [47]. This technology is sensitive, and cost effective. Detectors based on small high performance CCDs are cheap, yet offer high temporal resolution and information density and compatible with (and complementary to) MRI. It provides a different and rather more specific measure of the hemodynamic processes that drive fMRI, including blood oxygenation.

The complementary strengths and weaknesses of available functional neuroimaging techniques have driven efforts by a number of investigators to combine multiple imaging modalities. One of the most basic requirements for multimodality imaging is that it allows to define the spatial relationships between the measures. Since MRI is used to define the anatomy, the general strategy is to define the coordinate system of other measurements relative to the coordinate system of the MR volume imaging. The first step in multi-modality co-registration is to define the location of the sensor array relative to these anatomical landmarks. Integrated visualization based on multiple co-registered data sets is a useful application of multimodality imaging, allowing clinicians to appreciate the relationship between neuroanatomy and functional architecture. The same capabilities are essential for most other applications of integrated computational modeling.

A number of simultaneous comparative NIRS and fMRI studies have been conducted [71], [72], [16], [73],[74], [75]. These studies have addressed the problems of localization of detected signal and sensitivity of optical measurements to brain tissue. Some studies have shown a high temporal negative correlation

between BOLD and Hb responses [71]. Others confirm that the main aspect determining the time course of the BOLD signal in the human motor cortex during stimulation is due to the change in HB concentration and not the changes in regional CBV [76]. The rise in cerebral blood oxygenation is attributed to an increase in the regional CBF velocity, which occurs without a significant swelling of the blood vessels. The same group observed that the change in BOLD signal follows changes in rCBF with a time delay approximately equal to the ratio of the baseline values of the rCBV and rCBF [76].

The studies also show a good spatial collocation between BOLD and hemodynamic responses [77]. However, it is also observed that correlation between BOLD and Hb responses can be highly variable between subjects. Their study found that correlation between BOLD and HbO_2 were higher than between BOLD and Hb. This may be due to higher sensitivity of the optical measurement to changes in HbO_2.

1.6 Statistical Methods

1.6.1 Independent Component Analysis (ICA)

An unresolved problem in functional NIRS is the separation of functional signals from the contaminations by systemic and local physiological fluctuations. This problem was approached by using various signal processing methods, including the blind signal separation techniques [78].

Let us denote n recorded NIR signals $x_1(t), \ldots, x_n(t)$, where t is time. Under the assumption of small underlying changes each of these signals can be expressed as a weighted sum of the underlying components of brain haemodynamic activity $s_1(t), \ldots, s_n(t)$:

$$\begin{aligned} x_1(t) &= a_{1,1}s_{1,1} + \ldots + a_{1,k}s_{1,k} \\ &\vdots \\ x_n(t) &= a_{n,1}, s_{n,1} + \ldots + a_{n,k}s_{n,k} \end{aligned} \tag{1.8}$$

where $a_{1,1}$ and $a_{i,j}$ are some time-independent parameters. If we knew the parameters aij, we could solve the system of linear equations (1.8) for $s_1(t) \ldots s_n(t)$. A blind signal separation technique called Independent Component Analysis (ICA) estimates aij based on the assumption of the statistical independence of source signals $s_1(t) \ldots s_n(t)$.

1.6.2 Definition of ICA and fundamental properties of independence

The variables s_1 and s_2 are said to be independent if information on the value of s_1 does not give any information on the value of s_2, and vice versa [79]. Mathematically, independence can be defined by the probability densities. Let us denote by $p(s_1, s_2)$ the joint probability density function (PDF) of s_1 and s_2. Let us further denote by $p_1(s_1)$ the PDF of s_1 when it is considered alone: $p_1(s_1) = \int p(s_1, s_2) ds_2$

and similarly $p_2(s_2)$ for s_2. Then we define that s_1 and s_2 are independent if and only if the joint PDF is factorizable in the following way: $p(s_1, s_2) = p_1(s_1)p_2(s_2)$

This definition extends naturally for any number n of random variables, in which case the joint density must be a product of n terms. The definition can be used to derive a most important property of independent random variables. Given PDFs of two functions, h_1 and h_2, we always have $E\{h_1(s_1)h_2(s_2)\} = E\{h_1(s_1)\}E\{h_2(s_2)\}$

To rigorously define ICA [80]; [81], one can use a statistical latent variables model. Assume that we observe n linear mixtures $x_1, \ldots, x_n$ of n independent components

$$x_j = a_{j,1}s_1 + a_{j,2}s_2 + \ldots + a_{j,n}s_n; \;\; for \;\; all \;\; j_s. \tag{1.9}$$

We can assume that both the mixture variables and the independent components have zero mean: If this is not true, then the observable variables x_i can always be centered by subtracting the sample mean, which makes the model zero-mean.

Let us denote by x the random vector whose elements are the mixtures $x_1, \ldots, x_n$, and likewise by s the random vector with elements $s_1, \ldots, s_n$. Let us denote by A the matrix with elements $a_{i,j}$. Here, bold lower case letters indicate vectors and bold upper-case letters denote matrices. All vectors are column vectors; thus x^T, or the transpose of x, is a row vector. Using this vectormatrix notation, the above mixing model is written as

$$x = As \tag{1.10}$$

Sometimes we need the columns of matrix A; denoting them by a_j the model can also be written as

$$x = \sum a_i s_i \tag{1.11}$$

The statistical model in Equation (1.10) is called independent component analysis, or ICA model. The ICA model is a generative model, which means that it describes how the observed data are generated by a process of mixing the components s_i. Also the mixing matrix is assumed to be unknown. All we observe is the random vector x, and we must estimate both A and s using it. There are several general assumptions. The starting point for ICA is the very simple assumption that the components s_i are statistically independent and have non-Gaussian distributions . We do not assume these distributions known. For the simplicity, we also assume that the mixing matrix is square. After estimating A, we can compute its inverse, say W, and obtain the independent components as:

$$s = Wx \tag{1.12}$$

1.6.3 Uncorrelated variables are only partly independent

A weaker form of independence is uncorrelatedness. Two random variables s_1 and s_2 are said to be uncorrelated, if their covariance is zero: $E\{s_1s_2\} - E\{s_1\}E\{s_2\} = 0$. If the variables are independent, they are uncorrelated but uncorrelatedness does not imply independence.

1.6.4 Why Gaussian variables are forbidden

The fundamental restriction in ICA is that the independent components must be non-Gaussian for ICA to be possible. The non-gaussian distribution of two variables x_1 and x_2 contains information on the directions of the columns of the mixing matrix A: the colums of the mixing matrix could for example be located along the edges of the joint density of the variables (Figure 1.10, top view) [78].

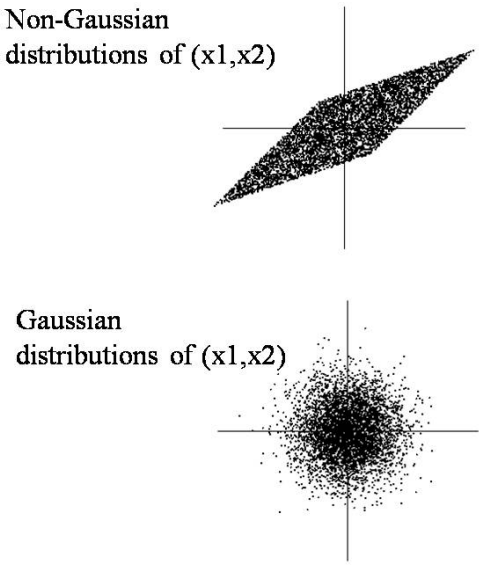

Figure 1.9: Examples of non-gaussian and gaussian distributions of two variables x_1 and x_2. From [78].

If x_1 and x_2 are Gaussian, uncorrelated, and of unit variance. Their joint density is completely symmetric. This probability density does not contain any information on the directions of the columns of the mixing matrix A. This is why A cannot be estimated. If just one of the independent components is Gaussian, the ICA model can still be estimated [78], [82].

1.6.5 Principles of ICA estimation

"Non-Gaussian is independent" [78]. The key to evaluation of independent component analysis is maximization of the non-Gaussianity of the variables. To estimate independent components, one should consider a linear combination of the x_i in Equation (1.12), where w is one of the rows of the inverse of A, a vector that maximizes the non-Gaussianity of $w^T x$. In practice, an algorithm would compute the direction in which the absolute value of the kurtosis of $s = w^T x$ is growing most strongly based on the available sample $x(1), \ldots, x(n)$, and use a gradient method or one of their extensions for finding a new vector w [78]. The landscape of nongaussianity could be searched in the n - dimensional space of the recorded signal. This space would have $2n$ local maxima, two for each IC. To find several independent components, all these local maxima should be found. This task is simplified by the requirement that the

different independent components are uncorrelated. We can always constrain the search to the space that gives estimates uncorrelated with the previous ones. This corresponds to orthogonalization in a suitably transformed (i.e. whitened) space.

A quantitative measure of estimation of non-Gaussianity of a random variable could be implemented by kurtosis or negentropy. Kurtosis is calculated as the fourth - order cumulant $kurt(s) = E[s^4]3(E[s^2])^2$, and it is zero for a Gaussian random variable. For most non-Gaussian random variables, kurtosis is non-zero, and it can be either positive or negative. Random variables that have a negative kurtosis are called sub-Gaussian, and those with positive kurtosis are called super-Gaussian. Huber (1985) showed that kurtosis is very sensitive to outliers and therefore not a robust measure of nongaussianity [82]. Thus, other measures of non-Gaussianity might be better than kurtosis in some situations. Negentropy that has properties that are opposite to those of kurtosis [78].

A second efficient measure of non-Gaussianity is given by negentropy, which is based on entropy. The differential entropy H of a random vector s with density $f(s)$ is defined as [83]; [84]:

$$H(s) = -\int f(s) log f(s) ds \tag{1.13}$$

A fundamental result of information theory is that a Gaussian variable has the largest entropy among all random variables of equal variance. This means that entropy could be used as a measure of non-Gaussianity because the Gaussian distribution is the most random or the least structured of all distributions. Entropy is small for distributions that are clearly concentrated on certain values, i.e. when the variable is clearly clustered, or has a PDF that is very spiky. To obtain a measure of non-Gaussianity that is zero for a Gaussian variable and always non-negative, one often uses a slightly modified version of the definition of differential entropy, called negentropy. Negentropy J is defined as follows: $J(s) = H(s_{gauss}) - H(s)$, where s_{gauss} is a Gaussian random variable of the same covariance matrix as s. A covariance matrix is a matrix whose element in the i, j position is the covariance between the ith and jth elements of a random variable [85]. Each element of the vector is a scalar random variable, either with a finite number of observed empirical values or with a finite or infinite number of potential values specified by a theoretical joint probability distribution of all the random variables. The entropy is largest for gaussian variables among all random variables of equal variance and could therefore be used as a measure for nongaussianity.

Another approach for ICA estimation can be based on the minimization of mutual information. It leads to the same principle of finding most non-Gaussian directions, i.e., finding new vectors w. In this approach, the independent components of a random vector x are calculated as an inverse transformation as in Equation (1.12), where the matrix $\boldsymbol{W}$ is determined so that the mutual information of the transformed components is minimized [78]. Another alternative of minimization of mutual information is the maximum likelihood estimation [78].

1.6.6 Preprocessing for ICA

Before applying an ICA algorithm, it is usually necessary to perform a preprocessing of the data which includes data centering and whitening. Centering x, means subtracting its mean vector $m = E\{x\}$ so as to make x a zero-mean variable.

Whitening means that before the application of the ICA algorithm (and after centering), the observed vector x can be transformed so that we obtain a new vector $\tilde{x}$ whose components are uncorrelated and their covariance matrix of $\tilde{x}$ is the identity matrix: $E\tilde{x}\tilde{x}^T = I$. The whitening transformation is always possible using the eigenvalue decomposition (EVD) of the covariance matrix $Exx^T = EDE^T$; where E is the orthogonal matrix of eigenvectors of Exx^T and D is the diagonal matrix of its eigenvalues [78].

Whitening can now be done by $\tilde{x} = ED^{-1/2}E^Tx$, where the matrix $D^{-1/2}$ is computed by a simple component wise operation.

Whitening transforms the mixing matrix into a new one, $\tilde{A}$. The utility of whitening results in the fact that the new mixing matrix $\tilde{A}$ is orthogonal. Whitening reduces the number of parameters to be estimated. Instead of having to estimate the n^2 parameters that are the elements of the original matrix A, we only need to estimate the new, orthogonal mixing matrix $\tilde{A}$. An orthogonal matrix contains $n(n-1)/2$ degrees of freedom. Thus one can say that whitening solves half of the problem of ICA.

1.6.7 FastICA algorithm

FastICA is a popular Matlab code implementing an ICA algorithm with data preprocessing. It was developed by [78].

The FastICA is based on the approximate calculation of negentropy for finding a maximum of the non-Gaussianity of w^Tx, [86]; [87].

The basic form of the FastICA algorithm is as follows:

1. Choose an initial (e.g. random) weight vector w
2. Let $w^+ = Exg(w^Tx) - E(g'(w^Tx)w$, where g is a non-quadratic function defined in [78]
3. Let $w = w^+ / \parallel w^+ \parallel$
4. If not converged, go back to 2

Note that convergence means that the old and new values of w point in the same direction, i.e. their dot-product is(almost) equal to 1. It is not necessary that the vector converges to a single point, since w and $-w$ define the same direction [78]. This is because the independent components can be defined only up to a multiplicative sign.

1.6.8 Properties of the FastICA algorithm

The FastICA algorithm and the underlying contrast functions have a number of desirable properties when compared with existing methods for ICA [78].

1. The convergence is cubic (or at least quadratic), under the assumption of the ICA data model. This is in contrast to ordinary ICA algorithms based on (stochastic) gradient descent methods, where the

convergence is only linear. This means a very fast convergence, as has been confirmed by simulations and experiments on real data.
2. Contrary to gradient-based algorithms, there are no step size parameters to choose. This means that the algorithm is easy to use.
3. The algorithm finds directly independent components of(practically) any non-Gaussian distribution using any non-linearity g. This is in contrast to many algorithms, where some estimate of the probability distribution function has to be first available, and the non-linearity must be chosen accordingly.
4. The performance of the method can be optimized by choosing a suitable non-linearity g. In particular, one can obtain algorithms that are robust and/or of minimum variance.
5. The independent components can be estimated one by one, which is roughly equivalent to doing projection pursuit. This is useful in exploratory data analysis, and decreases the computational load of the method in cases where only some of the independent components need to be estimated.
6. The FastICA has most of the advantages of neural algorithms: it is parallel, distributed, computationally simple, and requires little memory space. Stochastic gradient methods seem to be preferable only if fast adaptivity in a changing environment is required.
A Matlab implementation of the FastICA algorithm is available on the World Wide Web free of charge [88].

1.6.9 Applications of ICA

ICA has been applied to a number of different problems, especially in the field of neuroimaging. A brief overview of some of the research using ICA demonstrates the range of applicability of ICA implemented as either spatial (sICA) or temporal ICA (tICA). Of the many ICA applications, removal of blood flow artifacts in functional optical data [89], optical imaging of neurons [90], [91], and extracting task-related activation components from OT and fMRI data are some of the popular uses of this statistical approach [92], [93], [94].

Functional NIRS is sensitive to changes in detector-skin coupling associated with experimental procedure and extracerebral interference from the outer layers of the brain. Hence, signals recorded from the head are often contaminated with systemic noise and motion artifacts. ICA is one of the statistical methods used to address these issues. For example, Kohno [89] and Virtanen [95] were able to separate physiological interference and coupling artifacts from NIRS data by applying IC analysis to different channel configurations. In these studies, number of components were estimated based on the number of channels embedded in the probe. To our knowledge, there where no studies were ICA was performed on a single source-detector configuration.

Also, ICA can be used as an alternative to hypothesis driven approach to identify regions of activation, as in the case of fMRI studies, or to extract time courses of the original optical signal, in case of fNIRS studies. With ICA, such functional activation can be identified without a priori knowledge of expected hemodynamic responses [96], [97]. Limitation of these studies is that the choice of number of components is limited by the number of source-detector channels, and manufactured NIRS equipment, at least at the moment, operates at limited number of wavelengths. Therefore, method proposed in the second part of

the manuscript has a true novelty in processing NIR data.

1.7 General Linear Model (GLM)

Multiple regression analysis is a method for inference in the setting of linear relationships between a single response variable $\{y_i, x_{i1}, \ldots, x_{ip}\}_i = 1$ of n statistical units and multiple explanatory variables (p) [98]. A linear regression model assumes that the relationship between the dependent variable y_i and the p - vector of regressors is linear.

Let us denote the explanatory variables as $x_1, x_2, \ldots, x_p$. Then the statistical model for multiple linear regression is:

$$Y_i = \beta_0 + \beta_1 x_i 1 + \beta_2 x_i 2 + \ + \beta_p x_i p + \epsilon_i \tag{1.14}$$

for $i = 1, 2, \ldots, n$. The parameters of the model are $\beta_0, \beta_1, \beta_2, \ldots, \beta_p$. One can write these n equations in a vector form as $\boldsymbol{Y} = \boldsymbol{X\beta} + \boldsymbol{\epsilon}$, where

$$y = \begin{pmatrix} y_1 \\ y_2 \\ \vdots \\ y_n \end{pmatrix}, X = \begin{pmatrix} x_1' \\ x_2' \\ \vdots \\ x_n' \end{pmatrix} = \begin{pmatrix} x_{1,1} & \cdots & x_{1,p} \\ x_{2,1} & \cdots & x_{2,p} \\ \vdots & \ddots & \vdots \\ x_{n,1} & \cdots & x_{n,p} \end{pmatrix}, \beta = \begin{pmatrix} \beta_1 \\ \beta_2 \\ \vdots \\ \beta_p \end{pmatrix}, \epsilon = \begin{pmatrix} \epsilon_1 \\ \epsilon_2 \\ \vdots \\ \epsilon_n \end{pmatrix}$$

The subpopulation means describe the FIT part of the statistical model. The $RESIDUAL$ part represents the variation of observations about the means. Estimation of the multiple regression parameters is based on the principle of least squares. Let $b_0, b_1, b_2, \ldots, b_p$ denote the estimators of the parameters $\beta_0, \beta_1, \beta_2, \ldots, \beta_p$. For the ith observation, the predicted response is

$$\hat{Y_i} = b_0 + b_1 x_{i1} + b_2 x_{i2} + \ldots + b_p x_{ip} \tag{1.15}$$

The method of least squares chooses the values of the bs that make the sum of the squares of the residuals as small as possible.

$$\sum (y_i - b_0 - b_i x_{i1} - b_2 x_{i2} - \ldots - b_p x_{ip})^2 \tag{1.16}$$

The significance test for the multiple regression is the ANOVA F - test which tests the hypothesis that all of the regression coefficients, with the exception of the intercept, are 0. The degrees if freedom for the model are $df = p$ to reflect the fact that there are p explanatory variables. The sum of squares represent the sources if variation. The sum of squares and the degrees of freedom add: $SST = SSM + SSE$, $DFT = DFM + DFE$

The estimate of the variance σ^2 for the model is given by MSE. The ratio MSM/MSE is an F - statistics for testing the null hypothesis against the alternative hypothesis
$H_0 : \beta_1 = \beta_2 = \ldots = \beta_p = 0$
H_a : at least one of the β_j is not 0

The null hypothesis is that none of explanatory variables are predictors of the response variable when used in the form expressed by the multiple regression equation. The alternative hypothesis states that at least one of them is linearly related to the response. This does not mean that each predictor is statistically significant. The significance tests for individual regression coefficients assess the significance of each predictor variable assuming that all other parameters are included in the regression equation.

Squared multiple correlation coefficient, $R^2 = SSM/SST$, is the proportion of variation of the response variable y that is explained by the explanatory variables $x_1, x_2, \ldots, x_p$ in a multiple linear regression. The multiple regression model does not require any of the variables distributions to be normal. Only the deviations of the responses y from their means are assumed to be normal.

Chapter 2 presents a journal manuscript of two parts: first, optimal quantitation of the cerebral haemodymanic response in fNIRS is presented; second, independent component analysis applied to concomitant functional near infrared spectroscopy and fMRI data is discussed. The final Chapter presents conclusions and future work ideas.

Chapter 2

Journal Manuscripts

Optimal quantitation of the cerebral hemodynamic response in functional near-infrared spectroscopy

Irina Schelkanova and Vladislav Toronov*

Department of Physics, Ryerson University, 350 Victoria Street, Toronto, Ontario M5B 2K3, Canada

**toronov@ryerson.ca*

Abstract: We have compared cerebral hemodynamic changes measured by near-infrared spectroscopy (NIRS) with simultaneously acquired BOLD fMRI signals during breath hold challenge in humans. The oxy- and deoxyhemoglobin concentration changes were obtained from the same broadband NIRS data using four different quantitation methods. One method used only two wavelengths (690 nm and 830 nm), and three other methods used broadband data with different spectral fitting algorithms. We found that the broadband techniques employing spectral derivatives were significantly superior to the multi-wavelength methods in terms of the correlation with the BOLD signals. In two cases out of six we found that the time courses of the deoxyhemoglobin changes produced by the two-wavelength method were qualitatively inconsistent with the BOLD fMRI signals.

2.1 Introduction

In recent years many research groups began to use home-made or commercially available NIRS monitors in basic research on brain function and cognition [99], [100], [101], [102] and for clinical monitoring of the brain during and after cardiac surgery [103]. Most of these monitors have limited numbers of wavelengths. Monitors from NIRO family (Hamamatsu Photonics, Hamamatsu, Japan) use four wavelengths, while many, such as INVOS (Somanetics, Troy, MI) and ISS oximeters (ISS, Champaign, IL) use only two wavelengths of light. Such a multi-wavelength design based on non-dispersive light detectors, such as photomultipliers, was dictated by the availability and costs of the detectors in 1990. However the emergence of new generations of low-cost portable CCD spectrometers now allows for relatively inexpensive multichannel designs with broadband spectral resolution. Other options to achieve broadband spectral sensitivity are provided by acousto-optical [104] or liquid crystal tunable filters [105]. The goal of this study is to re-evaluate the capabilities of the broadband NIRS approach for cerebral perfusion monitoring in comparison with the multi-wavelength approach. We use a simple broad-band setup to measure cerebral responses to breatholding challenge in adult humans and compare our results with the simultaneously acquired blood oxygen level dependent (BOLD) functional MRI signals, which are indicative of the cerebral deoxyhemoglobin concentration changes Δ_{Hb}. Using different spectral analysis techniques we show that the best correlation between the BOLD fMRI and NIRS time courses occurs when Δ_{Hb} is obtained using an algorithm based on the spectral derivative fit of the attenuation.

The water and the deoxyhemoglobin spectral second derivative features were used in the past to quantify the chromophore concentration changes in human forearm [106] and the absolute deoxyhemoglobin concentration in the neonatal brain [107]. In both [106] and [107] the spectral derivative features were

only used to estimate the photon differential pathlengths. In this study we used spectral derivatives in a different fashion, namely we use them to calculate the chromophore concentration changes by fitting the first and the second spectral derivatives of the attenuation.

2.2 Materials and methods

2.2.1 NIRS

Near-infrared light was generated by a stabilized fan-cooled AvaLight-HAL Tungsten Halogen Light Source (Avantes Inc., Broomfield, CO) with an adjustable focusing connector to maximize light coupling with the source fiber. The source fibre bundle was made of 30 Thorlabs broadband silica $400mm$ core diameter fibers. On the probe side the source fibers were arranged circularly around the location of the detector bundle at a radius of $25mm$. Light was collected using a $3mm$ diameter fiber optic bundle (Sunoptic Technologies, FL). The length of all fibres was $6m$ so that the source and the detector could be set outside of the MRI scanner room. The detector bundle was connected to a QE65000 cooled spectrometer (Ocean Optics**,** Dunedin, FL), which had a spectral range between 650 and $1100nm$. The spectrometer output was digitized using the Spectral Suite software (Ocean Optics**,** Dunedin, FL).

The optical probe was positioned on the left side of the forehead near the hairline. Vitamin E capsules were attached to the probe for the visualization on MR images. A proper positioning against the frontal lobe avoiding sinuses was ensured using anatomical MRI. Spectra were acquired at the sampling rate of one spectrum per second. This sampling rate was selected to ensure that the instrumental noise does not affect physiological data.

2.2.2 MRI

Imaging was performed at Sunnybrook Health Sciences Centre using the Achieva $3.0T$ scanner with SENSE-Head-8 coil. In order to assess the position of the optical probe the $T2-$weighted, two-dimensional, turbo spin echo (T2W TSE; repetition time/echo time $3000/80ms$, 1 mm slice thickness, no gap, $22cm$ field of view, $\sim 0.43 \times 0.43 \times 1.00mm$ voxel size, $5.25 - min$ acquisition time) anatomical images were acquired. Functional images were taken during 360 seconds by EPI technique with $T2*-$weighted protocol (FE EPI sequence, $TR = 1000ms$, $TE = 35ms$, flip angle = $90deg$). The in-plane resolution was $1.72 \times 1.72mm^2$ (FoV = $22cm$ at 128×128 $pixel^2$), and 15 axial slices, each 4 mm thick.

2.2.3 Subjects and protocol

Breath holding was used because it generates blood CO_2 which increases BOLD signal as CO_2 acts as a cerebral vasodilator [108]. Vasodilation causes increased cerebral blood flow which washes the deoxyhemoglobin out of the cerebral capillary bed thus increasing both the cerebral blood volume and oxygenation [109]. Six young healthy adult females ($19 - 29$ years old) were placed into the scanner and audibly cued to perform a breath hold at the end of expiration with voluntary resumption of breathing after holding about 15-20 seconds. The exercise was repeated five times with 1 minute intervals. Research

has been performed according to Sunnybrook Guidelines applicable to MRI studies on healthy volunteers and to Ryerson University 2008-003-01 Research Ethics protocol.

2.2.4 Modeling

We assumed that changes in the normalized attenuation (ΔA) of near-infrared light in scattering tissue were governed by the Modified Beer Lambert Law:

$$\Delta A(\lambda, t) = \frac{1}{DP(\lambda)} \ln\left(\frac{I_0(\lambda)}{I_t(\lambda)}\right) = \varepsilon_{HbO2}(\lambda)\Delta_{HbO2}(t) + \varepsilon_{Hb}(\lambda)\Delta_{Hb}(t) \tag{2.1}$$

where $DP(\lambda)$ is the differential pathlength factor (DPF),$I_0(\lambda)$is the average intensity, $I_t(\lambda)$is the instantaneous intensity, $\varepsilon_{HbO2}$and $\varepsilon_{Hb}$are the oxy- and deoxy-hemoglobin extinction coefficients, respectively, and $\Delta_{HbO2}$and $\Delta_{Hb}$are the instantaneous hemoglobin concentration deviations from their average levels. We used the DPF dependence on the wavelength measured in [110] at normal fraction of inspired oxygen.

We used four different methods based on Eq. 1 to recover $\Delta_{HbO2}(t)$and $\Delta_{Hb}(t)$from our spectral data.

1. For two isolated wavelengths Eq.(2.1) reduces to a set of two linear equations with constant coefficients. We solved this system of equations for the wavelengths of $690nm$ and $830nm$ which are used in many bi-wavelength instruments. To reduce the noise the data were averaged within 5 nm wavebands centered at either 690 or $830nm$, respectively.

2. For the quasi-continuum of wavelengths between $690nm$ and $900nm$ we found instantaneous $\Delta_{HbO2}$and Δ_{Hb}using the general linear model (GLM) fit (*glmfit* function of MATLAB) of the instantaneous absorbance $\Delta A(\lambda, t)$.

3. To find $\Delta_{HbO2}$and Δ_{Hb}we also used the same GLM fit with the first spectral derivative of the instantaneous absorbance $\frac{\partial \Delta A(\lambda,t)}{\partial \lambda}$.

4. We used the GLM fit of the second spectral derivative of the instantaneous absorbance$\frac{\partial^2 \Delta A(\lambda,t)}{\partial \lambda^2}$ to obtain Δ_{Hb} only, since the second derivative of the oxy-hemoglobin extinction $\varepsilon_{HbO2}(\lambda)$is almost zero compared to that for$\varepsilon_{Hb}(\lambda)$.

The time series of the oxy- and deoxyhemoglobin changes obtained using the above four methods will be further referred to as the type $1-4$ signals and the correlations of those with BOLD will be referred to as type the $1-4$ correlations. We will also use the notations Δ_{Hb}^{1-4} to denote the deoxyhemoglobin signals obtained by Methods $1-4$.

In all methods using broadband data $(2-4)$ the parameters of *glmfit* were the same. Namely, the normal error distribution was assumed and the constant offset was set off. We found that the inclusion of the optional constant offset always produced unrealistically small $\Delta_{Hb}^2(t)$ changes (less than $0.01mM$). Without using the offset in *glmfit* all $\Delta_{Hb}(t)$ amplitudes were always within $0.5-1mM$. In Methods 3 and 4 the spectra were smoothed using *smooth* function with a $3nm$ span in order to reduce the effect

of the spectral noise. This size of the span produced $\Delta^{3,4}_{Hb}(t)$and$\Delta^{2,3}_{HbO2}(t)$ of similar amplitudes to those of $\Delta^{1,2}_{Hb}(t)$and$\Delta^{1,2}_{HbO2}(t)$.

2.2.5 Noise analysis

In order to test how Δ_{Hb} signals produced by different methods were affected by the instrumental noise we have performed the power spectrum analysis of the noise and physiological signals. The instrumental noise was acquired on a tissue-like phantom (ISS, Champaign, IL) using the same instrumentation and acquisition settings as those used for the physiological acquisitions. Due to the optical properties of the phantom the spectral intensity values of the phantom signal were in the same range of values as the for the in-vivo signals. Figure 2.1(a) compares the power spectra of all four types of Δ_{Hb}obtained from the phantom data. Although a much smaller number of photons contributed to the type 1 signal than to other signals, from Figure 2.1(a) one can see that the noise influence was strongest for the type 3 and 4 signals. This was both due to the relatively low sampling frequency and due to the higher spectral noise in the first and second order spectral derivatives of the absorbance spectra than in the absorbance itself. However, as Figure 2.1(b) shows, during the in-vivo measurements the instrumental noise was insignificant compared to the physiological signals. Figure 2.1(b) compares the temporal power spectra of the raw data acquired on the phantom and *in-vivo*. The plotted power spectral densities correspond to the frequency of the breath holding repetitions ($0.017Hz$) as functions of the wavelength. In order to quantitatively compare the signal and the noise power spectra both spectra were normalized to the corresponding time-averaged spectral intensities. From Figure 2.1(b) one can see that in the range between 690 and 900 nm the signal to noise ratio was much greater than one. In particular, it was close to four near 690 nm and close to 60 near 800 nm. This confirms that none of the four types of derived hemodynamic responses were significantly affected by the instrumental noise.

2.2.6 Comparison between NIRS and BOLD MRI

Although a number of studies (see for example [73]) have revealed that BOLD signal most closely corresponds to the negative of $\Delta_{Hb}(t)$, we compared BOLD signals both with the changes in the deoxy-hemoglobin and oxyhemoglobin concentrations obtained by the above four methods. For this we used the correlation analysis tools implemented in AFNI software [111]. Before applying the correlation analysis the fMRI data sets were preprocessed to correct for motion artifacts and slice timing differences and to remove non-brain regions. Then both fMRI and NIRS time series were filtered using the digital filter with the pass band between 0.01 and 0.02 Hz corresponding to the breath hold repetition frequency. The Butterworth filter was designed using the MATLAB signal processing tool and applied to the data time series using the *filtfilt* function to prevent temporal shifts of filtered signals. Then the correlation coefficients between -$\Delta_{Hb}(t)$, $\Delta_{HbO2}(t)$ and the voxel BOLD signals were computed for voxels within the volume of the brain interrogated by the optical channel. Each such a volume of interrogation included approximately 1000 fMRI voxels. Following the approach used in [112] and [113] we determined the volume of interrogation for each measurement using the voxel photon-hitting density P_n defined by Eq.

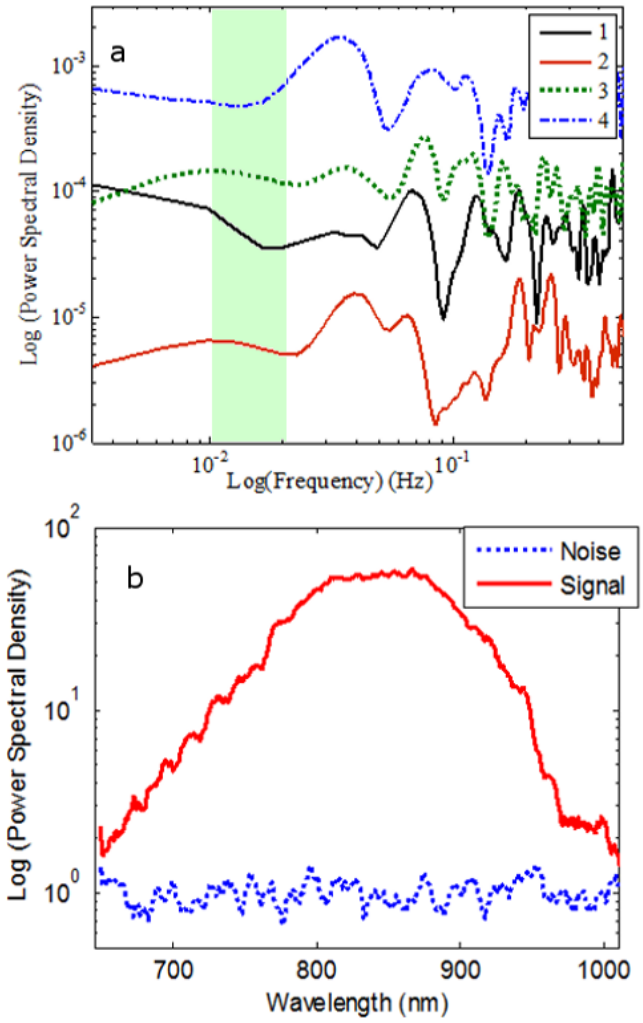

Figure 2.1: (a) Temporal power spectra of noise for all four types ofΔ_{Hb}. Numbers 1 through 4 in the legend correspond to the type of the signal. The bar shows the spectral band of the signal due to repeated breath holdings. (b) Normalized power spectral densities of noise (acquired on the phantom) and cross-subject average signal (acquired on a subject during breath hold exercise) at $0.017Hz$.

(2.1) in [112]. Only voxels with P_n >0.1 $max(P_n)$ were included into the interrogation volume. The average correlation coefficients and the average BOLD signals were computed using the equation

$$\bar{X} = \sum_{v} x_n \cdot W_n \tag{2.2}$$

where W_n =$P_n/\Sigma P_n$, where x_n was the voxel correlation or BOLD intensity and $\bar{X}$ was the corresponding volume average quantity. For the analysis of the statistical significance of the average correlation the

Table 2.1: Volume-averaged correlation coefficients for all subjects: three types of $\Delta_{HbO2}(t)$ **and four types of** $-\Delta_{Hb}(t)$**. The corresponding confidence intervals were all close to** $\pm$**0.01**

Subject	**type 1**		**type 2**		**type 3**		**type 4**
	HHb	HbO_2	HHb	HbO_2	HHb	HbO_2	HHb
1	0.22	0.75	-0.43	0.78	0.72	0.77	0.56
2	0.38	0.67	0.41	0.70	0.52	0.71	0.47
3	0.51	0.72	0.64	0.74	0.67	0.81	0.53
4	-0.03	0.56	0.29	0.61	0.41	0.59	0.34
5	0.59	0.61	-0.14	0.65	0.68	0.63	0.59
6	0.07	0.68	0.43	0.71	0.52	0.59	0.49
Group	0.29	0.67	0.20	0.70	0.59	0.68	0.45

t-test was applied to the W_n -weighted voxel correlations.

2.3 Results

Figure 2.2(a) shows the time courses of -$\Delta_{Hb}(t)$ (negative of deoxyhemoglobin concentration change) for one of six subjects. Numbers 1 through 4 in the legend correspond to four different methods to obtain$\Delta_{Hb}(t)$. Figure 2.2(b) shows the BOLD signal averaged over the volume near the optical probe (see Figure 2.3). In Fig. 2.2(a) one can see that although all curves showed similar amplitudes of changes and a certain degree of synchronicity with the exercise, their time courses were visibly different. While green and blue curves in Figure 2.2(a) were well in phase with the BOLD signal shown in Figure 2.2(b) (the correlation values were 0.72 and 0.56, respectively, see Table 1), the red curve was anti-correlated with BOLD (correlation value of -0.43), and the black curve was not well-correlated with BOLD (correlation value of 0.23). However, all three $\Delta_{HbO2}(t)$ shown in Fig. 2 (c) were well correlated with the average BOLD signal (correlations of 0.75 and higher for this subject). We did not observe significant differences in the amplitudes of neither $\Delta_{HbO2}(t)$nor $\Delta_{Hb}(t)$ obtained by different methods.

Figure 2.3 shows one slice of the functional image obtained by correlating $-\Delta^3_{Hb}(t)$with the voxel BOLD signals. The voxels shown by colors were within the volume interrogated by the light channel. Red color corresponded to high positive correlation, and blue color corresponded to high negative correlation. One can see that although most of voxels showed positive correlation between BOLD and $-\Delta^3_{Hb}(t)$, some voxels showed negative correlations.

2.4 Discussion

We have computed cerebral oxy- and deoxyhemoglobin responses to breath hold challenge from the same broadband near-infrared data using four different methods. The first method used only two wavelengths, and three other methods used broadband data with different spectral fitting algorithms. The

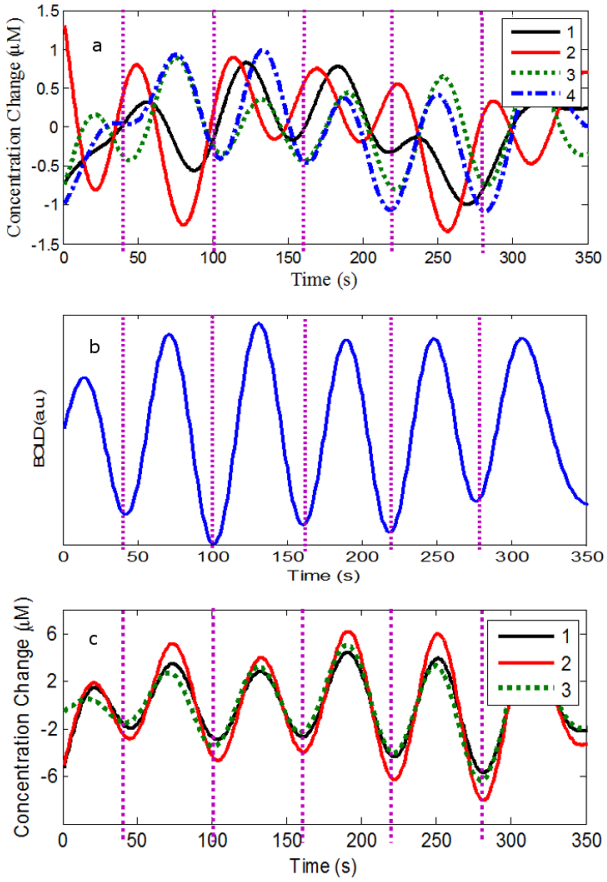

Figure 2.2: (a)Time courses of $-\Delta_{Hb}(t)$ for one of six subjects. Numbers 1 through 4 in the legend correspond to four different methods to obtain $\Delta_{Hb}(t)$. The vertical lines show the beginning of each breath hold. (b) Volume - average BOLD signal (c) Time courses of $\Delta_{HbO2}(t)$ for the same measurement.

$\Delta_{HbO2}(t)$signals were always well synchronized with the BOLD signal. Unlike $\Delta_{HbO2}(t)$, in some cases the behaviors of $-\Delta^1_{Hb}(t)$ and $-\Delta^2_{Hb}(t)$were qualitatively different from the time courses of the volume-average BOLD signals and of $-\Delta^3_{Hb}(t)$ and $-\Delta^4_{Hb}(t)$. The latter were always consistent with the time course of the average BOLD signals. At a group average level all four methods were qualitatively consistent with BOLD in terms of the sign of the correlation. However, the group average correlations for $-\Delta^3_{Hb}(t)$ and $-\Delta^4_{Hb}(t)$ were higher than for $-\Delta^1_{Hb}(t)$ and $-\Delta^2_{Hb}(t)$, and the corresponding confidence intervals did not overlap. One should emphasize that methods 3 and 4 were essentially broadband ones as they used spectral derivatives of the absorbance changes.

The methods that used the spectral derivatives were more prone to temporal instrumental noise because the fitting procedures converted the spectral noise into the temporal one. However the same methods produced -$\Delta_{Hb}(t)$ signals that were better correlated with the BOLD signals than two other methods. The highest group correlation was obtained using the first spectral derivative and the worst

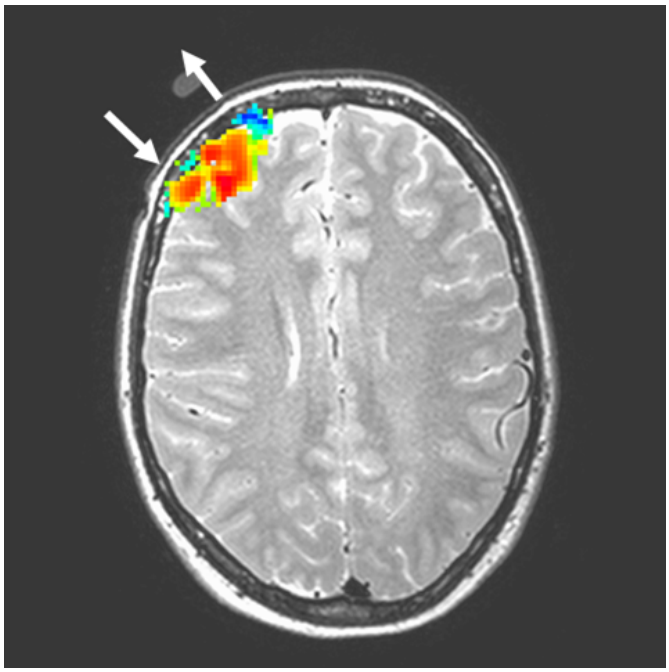

Figure 2.3: BOLD-NIRS Correlation map. Red color corresponds to high positive correlation, and blue color corresponds to high negative correlation. The arrows show the positions of the light source and detector.

correlation was produced by the direct spectral absorbance fit (Method 2). Both Methods 2 and 3 used the same mathematical fitting algorithm, i.e. the GLM fit, but were applied either to the absorbance change (Method 2) or to the spectral derivative of it (Methods 3). The reason for such a contrast behavior of these two similar methods should was twofold. The first part of the reason was physiological and consisted in the opposite directions of changes in the oxy- and deoxyhenoglobin concentrations due to the washout effect [109]. The increases in the oxyhemoglobin concentration caused the entire absorbance spectrum to increase but with greater effect in the longer wavelength half of the used spectral band (wavelengths greater than 800 nm). The decreases in the deoxyhemoglobin concentration cased the opposite effect on the absorbance but mostly in the short-wavelength part of the spectrum (wavelengths from 700 to 800 nm). Since the concentration of the deoxyhemoglobin in the brain was much lower than the concentration of the oxyhemoglobin, the relative changes in the former were also much smaller than in the latter. Therefore the overall rise of the absorption across the spectral band 700-900 nm was much stronger than the differences between the short- and the long-wavelength halves of the band. These differences in the effects of the oxy- and deoxyhemoglobin changes on the absorbance spectrum could result in a poor quantitation of $\Delta_{Hb}(t)$by Methods 1 and 2 in the cases when signal distortions due to physiological or motion artifacts occurred. These distortions did not affect significantly $\Delta_{HbO2}(t)$because of the larger amplitude of $\Delta_{HbO2}(t)$changes. However, the effect of $\Delta_{Hb}(t)$and$\Delta_{HbO2}(t)$ on the spectral derivatives of the absorbance was better balanced than that on the

absorbance itself because the differentiation eliminated the homogeneous changes across the spectrum and magnified the effect of the deoxyhemoglobin concentration changes due to the strong feature in the first- and second-order differential extinction spectra of deoxihemoglobin near 760 nm (see Figure 6 in [106]).

The second differential extinction spectrum of the deoxyhemoglobin had even stronger feature near 760 nm than the first differential spectrum and therefore in terms of $\Delta_{Hb}(t)$ Method 4 theoretically could provide even better result than Method 3. However, since the second differential also magnified the spectral noise, the Method 3 provided the best performance. The two-wavelength Method 1 worked slightly better than the broadband Method 2 because the algorithm differences. The algorithm of Method 1 was based not on the fitting of the absorbance changes spectrum but rather on the solution of the linear system of equations for the absorption changes at 690 nm and 830 nm. At these two wavelengths the difference between the extinction spectra of HHb and HbO_2 were high and in particular at the 690 nm the HbO_2 extinction was minimal so that the effect of HbO_2 changes at 690 nm was much smaller than the effect of HHb changes. However, both Method 3 and 4 outperformed Method 1 in terms of $\Delta_{Hb}(t)$ quantitation.

In [95] the principal and the independent component analyses (PCA and ICA, respectively) were used to clean the distorted hemodynamic signals measured by a two-wavelength system at 30 mm source-detector separations during breath holding. Both PCA and ICA produced better signals in cases of slight distortions, i.e. when typical exercise-synchronized increases in $\Delta_{HbO2}(t)$ and decreases in $\Delta_{Hb}(t)$ were noticeable in non-cleaned data. However, these methods would not improve the behavior of "bad" signals such as the red curve in Figure 2.2, a in our case unless more channels with different source-detector separations were used. Nevertheless, if the underlying reasons for a bad performance of Methods 1 and 2 were the data artifacts such as the hemodynamic fluctuations in the scalp, there is a chance that the cerebral signals acquired using two-wavelength methods can be cleaned if the distortions were isolated, for example by applying advanced signal processing techniques to the data acquired at short and long source-detector distances. On the other hand, our results show that our broadband Method 3 at least provides a single-channel alternative to PCA and ICA which require multi-channel measurements.

2.5 Conclusions and future work

We have compared cerebral hemodynamic signals obtained using near-infrared spectroscopy (NIRS) with simultaneously acquired BOLD fMRI signals during breatholding challenge. The oxy- and deoxyhemoglobin concentration changes were obtained from the same broadband NIRS data using four different quantitation methods. One method used only two wavelengths, and three other methods used broadband data with different spectral fitting algorithms. We have found that broadband techniques using spectral derivative algorithms were superior over the multi-wavelength methods in studies of cerebral hemodynamic responses to stimuli in humans.

In our future work we plan to apply the independent and principal component analyses to the broadband data acquired at multiple source-detector distances such that the contribution of the scalp

can be separated from the cerebral signals. This should clarify whether the advanced signal processing techniques applied to the multi-distance data will be sufficient to resolve the problems of the two-wavelength method or the broadband approach is required to ensure the correct measurement of cerebral deoxyhemoglobin changes.

Independent component analysis of concomitant functional near infrared spectroscopy and magnetic resonance imaging data

Irina Schelkanova and Vladislav Toronov*

Department of Physics, Ryerson University, 350 Victoria Street, Toronto, Ontario M5B 2K3, Canada

**toronov@ryerson.ca*

Abstract:

Although near infrared spectroscopy (NIRS) is now widely used both in emerging clinical techniques and in cognitive neuroscience [114], the development of the apparatuses and signal processing methods for these applications is still a hot research topic. One of the main issues of functional NIRS is the separation of functional signals from the contaminations by systemic and local physiological fluctuations. Various signal processing methods, including independent component analysis (ICA) [78], were applied to the data acquired at the same wavelength and at multiple sites on the human or animal heads [115] during functional activation. These signal processing procedures resulted in a number of independent components that could be attributed to functional activation but their physiological meaning remains unknown. Moreover, the best physiological specificity is provided by broadband NIRS [77]. A comparison with functional magnetic resonance imaging (fMRI) allows determining the spatial origin of fNIRS signals [77]. In this study, we applied ICA to broadband NIRS data to distill the components which might correspond to the breath hold activation paradigm and to correlate their time courses with the simultaneously acquired fMRI signals. Although the original signals were quite diverse, we found very few different components. The components correlated highly with fMRI BOLD signal at different locations in the brain.

2.6 Introduction

Although near infrared spectroscopy (NIRS) is now [21]widely used both in emerging clinical techniques and in cognitive neuroscience[114], the development of the apparatuses and signal processing methods for these applications is still a hot research topic. The main unresolved problem in functional NIRS is the separation of functional signals from the contaminations by systemic and local physiological fluctuations. This problem was approached by using various signal processing methods, including blind signal separation techniques[116]. In particular, principal component analysis (PCA) and independent component analysis (ICA)[78] were applied to the data acquired at the same wavelength and at multiple locations on the human or animal heads [115] during functional activation. These signal processing procedures resulted in a number of principal or independent components that could be attributed to functional activity but their physiological meaning remained unknown. On the other hand, the best physiological specificity is provided by broadband NIRS [77]. Also, a comparison with functional magnetic resonance imaging (fMRI) allows determining the spatial origin of fNIRS signals [77]. In this study

we applied PCA and ICA to broadband NIRS data to distill the components correlating with the breath hold activation paradigm and compared them with the simultaneously acquired fMRI signals. Breath holding was used because it generates blood carbon dioxide (CO_2) which increases the blood-oxygen-level-dependent (BOLD) signal as CO_2 acts as a cerebral vasodilator. Vasodilation causes increased cerebral blood flow which washes deoxyhaemoglobin out of the cerebral capillary bed thus increasing both the cerebral blood volume and oxygenation. Although the original signals were quite diverse, we found very few different components which corresponded to fMRI signals at different locations in the brain and to different physiological chromophores.

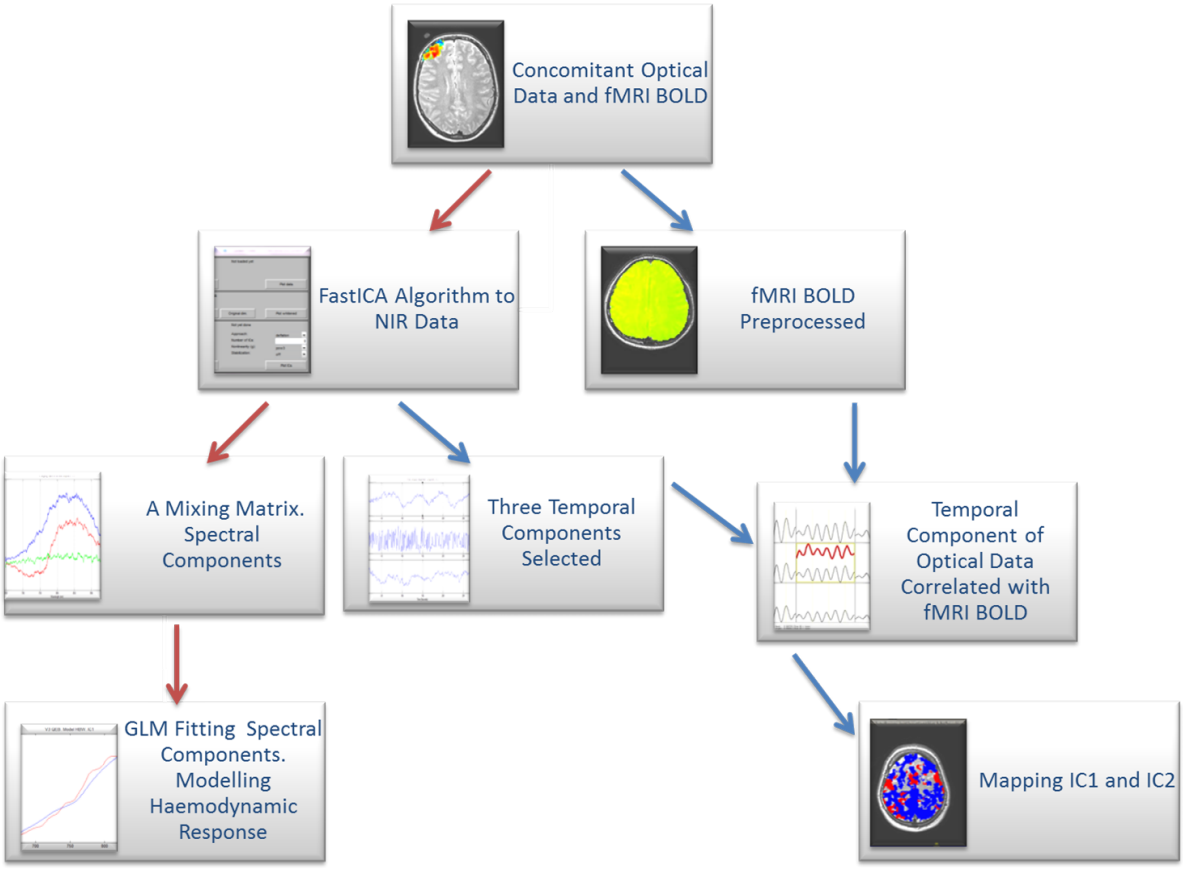

Figure 2.4: Schematic diagram of data analysis

2.7 Method

2.7.1 Participants and Experimental Paradigm

Optical data was obtained in two separate sessions from 8 healthy adult participants (V1-V8; 1 male, 7 females; 19 - 29 years old), all of whom were right-handed. All participants gave informed consent before participation and the experiment has been performed according to Sunnybrook Guidelines applicable to MRI studies on healthy volunteers and to Ryerson University 2008-003-01 Research Ethics protocol. The data sets used in this study were the same data described in[117]. Participants were placed into the scanner and audibly cued to perform a breath hold at the end of expiration with voluntary resumption of breathing after holding for about 15-20 seconds. The exercise was repeated five times with 40-second rest intervals.

2.7.2 Data Acquisition

Near-infrared light was generated by a stabilized fan-cooled AvaLight-HAL Tungsten Halogen Light Source (Avantes Inc., Broomfield, CO) with an adjustable focusing connector to maximize light coupling with the source fiber. The source fibre bundle was made of 30 Thorlabs broadband silica 400 μm core diameter fibers. On the probe side the source fibers were arranged circularly around the location of the detector bundle at a radius of 25 mm. Light was collected using a 3-mm diameter fiber optic bundle (Sunoptic Technologies, FL). The length of all fibers was 6 m so that the source and the detector could be set outside of the MRI scanner room. The detector bundle was connected to a QEB65000 cooled spectrometer (Ocean Optics, Dunedin, FL), which had 1044 wavelength channels in a spectral range between 650 and 1100 nm. The spectrometer output was digitized using the Spectral Suite software (Ocean Optics, Dunedin, FL).

The optical probe was positioned on the left side of the forehead near the hairline. A Vitamin E capsule was attached to the probe for visualization on MR images. A proper positioning against the frontal lobe avoiding sinuses was ensured using anatomical MRI. Spectra were acquired at the sampling rate of one spectrum per second. This sampling rate was selected to ensure that the instrumental noise would not affect physiological data and to match the acquisition rate of the MR scanner.

MR imaging was performed at Sunnybrook Health Sciences Centre using the Achieva 3.0 T scanner with SENSE-Head-8 coil. In order to assess the position of the optical probe, T2-weighted, two-dimensional, turbo spin echo (T2W TSE; repetition time/echo time 3000/80 ms, 1-mm slice thickness, no gap, 22-cm field of view, 0.43 x 0.43 x 1.00 mm voxel size, 5.25-min acquisition time) anatomical images were acquired. Functional images were taken during 360 seconds by EPI technique with T2*-weighted protocol (FE-EPI sequence, TR = 1000 ms, TE = 35 ms, flip angle = 90 deg). The in-plane resolution was 1.72 x 1.72 mm2 (FoV = 22 cm at 128 x 128 pixels), and 15 axial slices, each 4 mm thick.

2.7.3 Signal Processing

Near Infrared Data Processing. Independent Component Analysis (ICA) Algorithm and General Linear Model (GLM)

As a preprocessing step, the NIRS data were detrended using *poldetrendM* MATLAB function (MATLAB Mathworks, Inc). Then we used the FastICA algorithm[78] [118] to separate optical signals on 970 NIRS spectral channels (650-1000 nm) on the time structure of data (temporal ICA) (Figure 2.5). Identified temporal components were smoothed using smooth MATLAB function with 10 temporal points in order to reduce the effect of the noise.

In a NIR signal matrix rotation, A, the mixing matrix, represents mixed spectra of the temporal components (Figure 2.5). Selected spectra were smoothed over a span of 10 nm. For the quasi-continuum of wavelengths between 650 nm and 850 nm we used the general linear model (GLM) fit (*glmfit* function of MATLAB) to identify composition of the spectra. The time courses of selected spectral components of A weighting matrix were compared with fMRI signals using a correlation analysis tool implemented in AFNI software[119]. Colour coded spatial mapping of the components was done using AFNI software (Figure 2.9).

fMRI (BOLD) Preprocessing

The fMRI data sets were preprocessed to correct for motion artifacts, slice timing differences, remove non-brain regions and perform functional registration to the anatomical images. Then both fMRI and NIRS time series were filtered using the digital filter with the pass band between 0.01 and 0.04 Hz.

2.8 Results

Optical data of all participants were separated into three temporal independent components. Figure 2.5 (A) shows the output of the FastICA algorithm for a representative NIR data of volunteer 3 (V3). For all data sets, it was observed that the choice of three components was the optimal one, as very similar time series were evident: two time courses which followed the expected haemodynamic responses but in different directions, and an apparent noise. The number of independent components was chosen based on an iterative approach, and the fact that three components contained above 70 percent of information available in the data.

One of the resulting outputs of the ICA is the A mixing matrix. For the NIR data, this matrix contains spectral information of the temporal components. We observed two stable spectra (Figure 2.5 (B)), which can be a consequence of the breath hold exercise. The same spectral features were found in all data sets. As we observed repeated shapes, the two spectral components were selected for further analysis. Figure 2.6 and Figure 2.7 are plots of the selected components for the first four subjects. Based on the distinct forms of the components, the components were assigned IC1 (blue line) and IC2 (red line) codes.

As we were interested in investigating the relationship between temporal courses of NIR data and

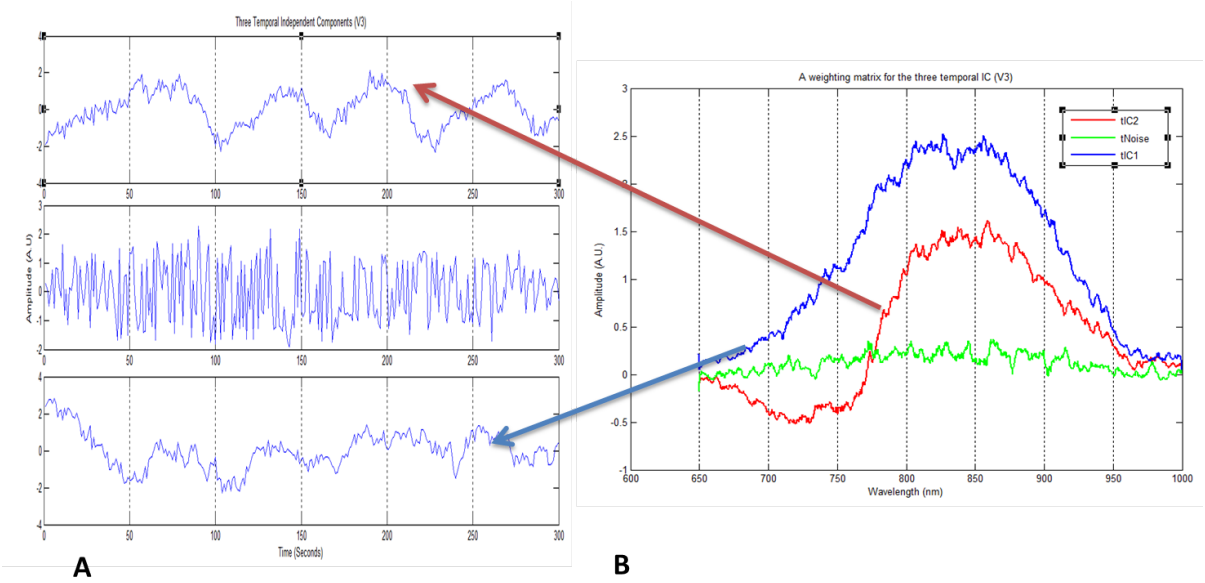

Figure 2.5: (A) NIR data separated into three temporal independent components for a subject S3. (B) *A* mixing matrix for the corresponding temporal components. Arrows link the corresponding time-spectrum connection.

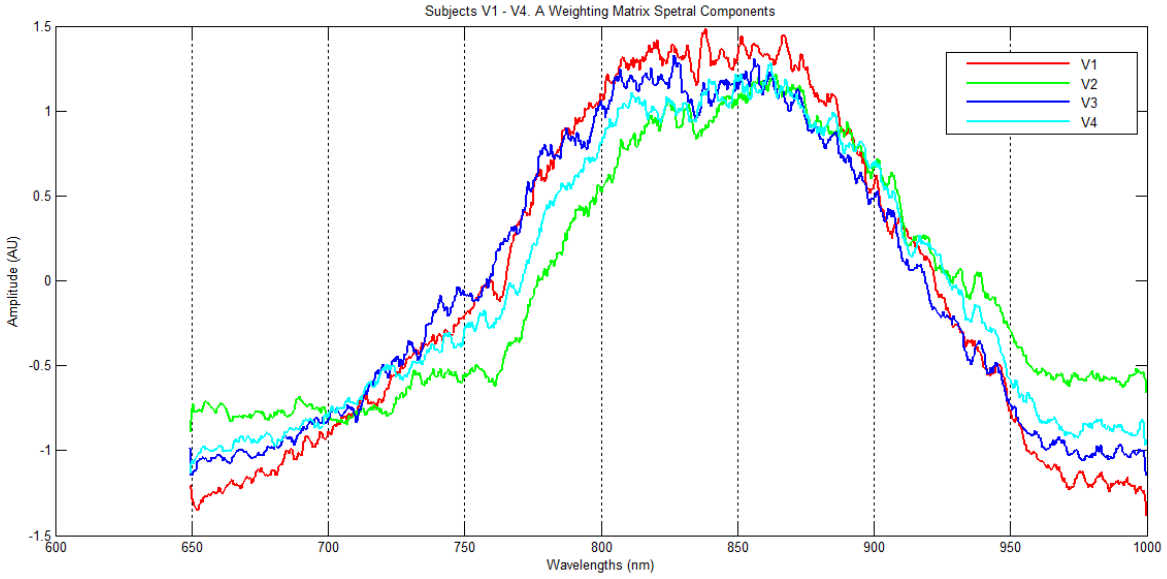

Figure 2.6: Spectral component (IC1) of the A mixing matrix for the first four volunteers (V1 - V4)

fMRI signal, temporal components of the selected forms were correlated with BOLD time course. Although NIR light interrogates only a fraction of the brain volume, the selected time courses were cor-

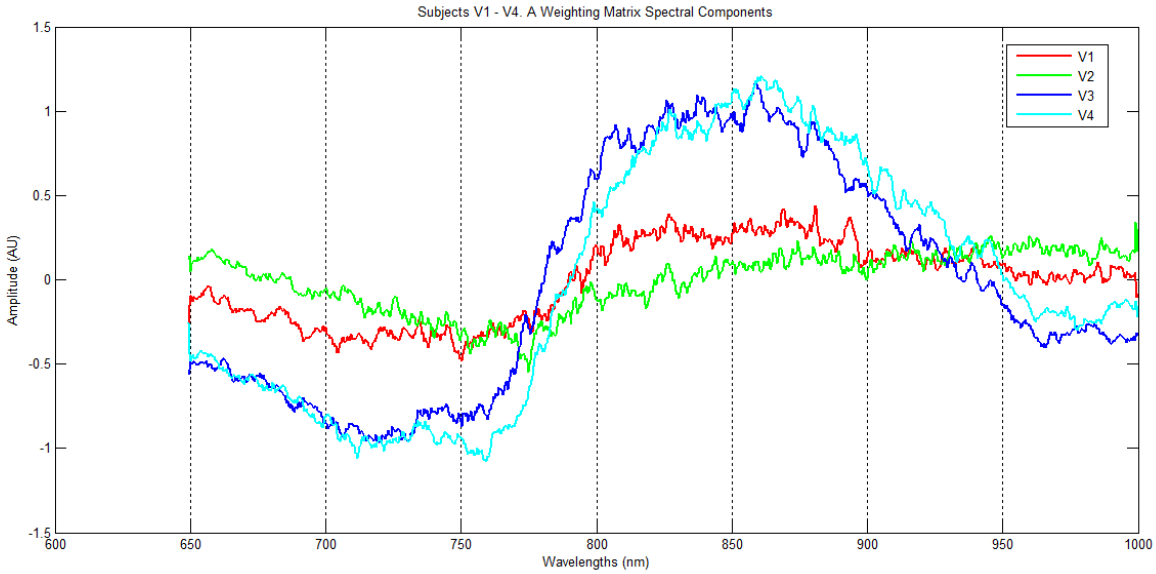

Figure 2.7: Spectral component (IC2) of the A weighting matrix for the first four volunteers (V1 - V4)

related to each voxel of the brain. Table 2.2 summarizes the ranges of correlation coefficients for each subject of the study for both temporal components. In seven out of eight correlated data sets, the components were non-overlapping, which is marked by the letter N next to the numbering of the participants.

After comparing spatial distributions of correlation coefficients for each of the components, we found that by setting an appropriate threshold, separation of the components into unique spatial regions is possible (Figure 2.8).

Five slices in Figure 2.9 correspond to the maximum depth which near infrared light can penetrate in the adult head. Blue coloured mask indicates the regions of correlation coefficients of IC1 below negative 0.60. Red coloured mask contains the information for the IC2 above the threshold of positive 0.45. The direction of the temporal components is estimated relative to BOLD.

Next, we wanted to identify the physiological composition of the spectral components. Five chromophores visible through the optical window were linearly combined into eight models and fitted in the IC1 (Figure 2.10) and IC2 (Figure 2.11). Absorption coefficients for all chromophores were extracted from [120].

Eight models:

DHB only deoxyhaemoglobin ;

HB oxy- and deoxy haemoglobin

HBW - oxy- and deoxy haemoglobin and water

HBWC - oxy- and deoxy haemoglobin , water, and cytochrome oxidase

Table 2.2: For all participants (V1 - V8). For IC1 and IC2 ranges of correlation coefficients. Capital letter N indicates that for that subject the two components have non-overlapping distributions of correlation coefficients

Subjects	IC	Correlation Coefficients Range	Subjects	IC	Correlation Coefficients Range
V1/N	**1**	**-0.9192 - 0.8301**	**V5/N**	**1**	**-0.6339 - 0.6291**
	2	**-0.6977 - 0.7107**		**2**	**-0.7667 - 7615**
V2/O	**1**	**-0.7738 - 0.7255**	**V6/N**	**1**	**-0.9153 - 0.8437**
	2	**-0.754 - 0.7444**		**2**	**-0.8588 - 0.6717**
V3/N	**1**	**-0.8097 - 0.7285**	**V7/N**	**1**	**-0.7397 - 0.7569**
	2	**-0.5409 - 0.6091**		**2**	**-0.5216 - 0.5738**
V4/N	**1**	**-0.8173 - 0.7964**	**V8/N**	**1**	**-0.9226 - 0.8858**
	2	**-0.82 - 0.8316**		**2**	**-0.8428 - 0.8696**

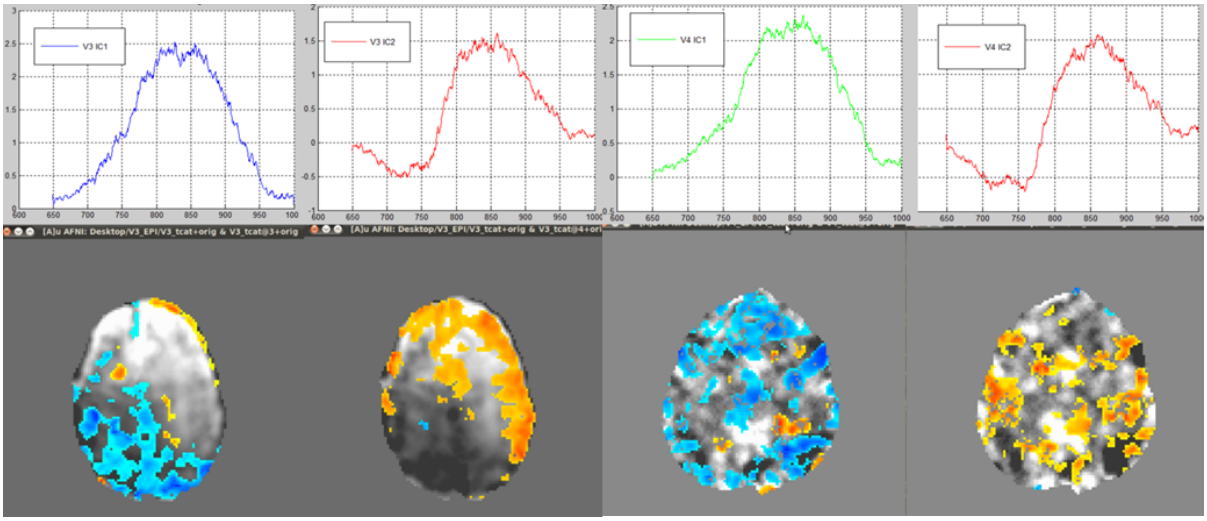

Figure 2.8: Exemplary images of correlation coefficient distributions for subjects V3 and V4. Top panel: two spectral components shown above its respective unique spatial distributions of correlation coefficients. Correlation coefficients (CC) displayed are above the threshold of the absolute value of 0.45

HBC - oxy- and deoxy haemoglobin , and cytochrome oxidase

HBWR - oxy- and deoxy haemoglobin , water, and reduced cytochrome oxidase

HBR - oxy- and deoxy haemoglobin , and reduced cytochrome oxidase

Full Model - oxy- and deoxy haemoglobin , water, cytochrome oxidase, and reduced cytochrome oxidase

We conducted linear regression analysis to determine and to compare statistical significance of the models. The correlation coefficients (R and R^2) of the nine models fitted into IC1 and IC2 reduced spectra are displayed in Figures 2.10 and Fugure 2.11.

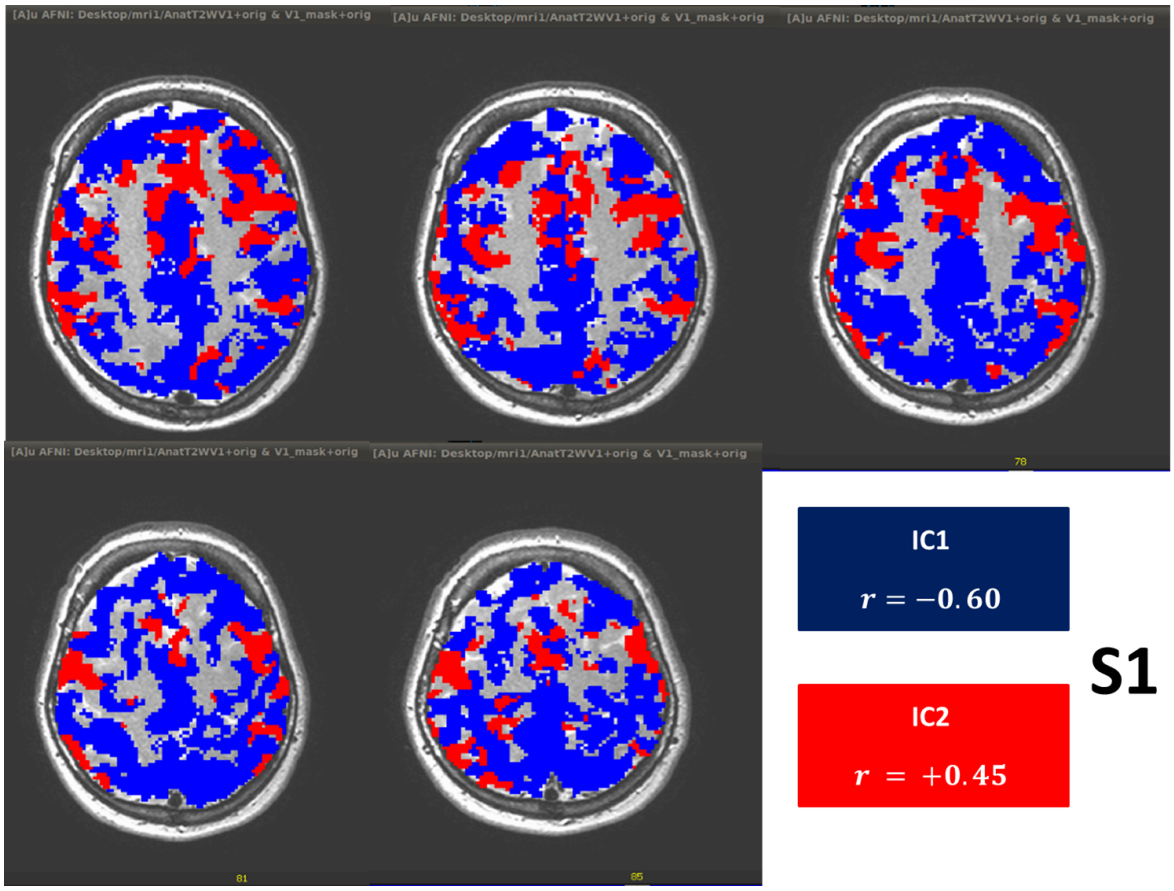

Figure 2.9: Colour coded spatial mapping of the temporal components for S1. The colour indicates direction of the signal relative to BOLD.

2.9 Discussion

In each of the eight volunteers, the FastICA algorithm produced temporal components corresponding to the expected haemodynamic response for the breath hold challenge. The advantage of ICA over the conventional haemodynamic theory driven approach is that it can be used to investigate haemodynamic responses even if the response is not known. NIR data is a composition and superposition of many physiological signals, precise formulation of which is challenging. For example, Figure 2A shows three temporal components extracted from the optical data. It is apparent that although the first and the third signals both follow the expected time course of the breath hold exercise, the signals have different time courses, and physiological origin of these particular responses is not known. The middle panel signal was treated as noise. However, the ICA technique separates signals based on statistical independence and thus physiological importance of the signals cannot be determined from components alone. To search for explanation of the observed components we looked at the spectral information contained in the A

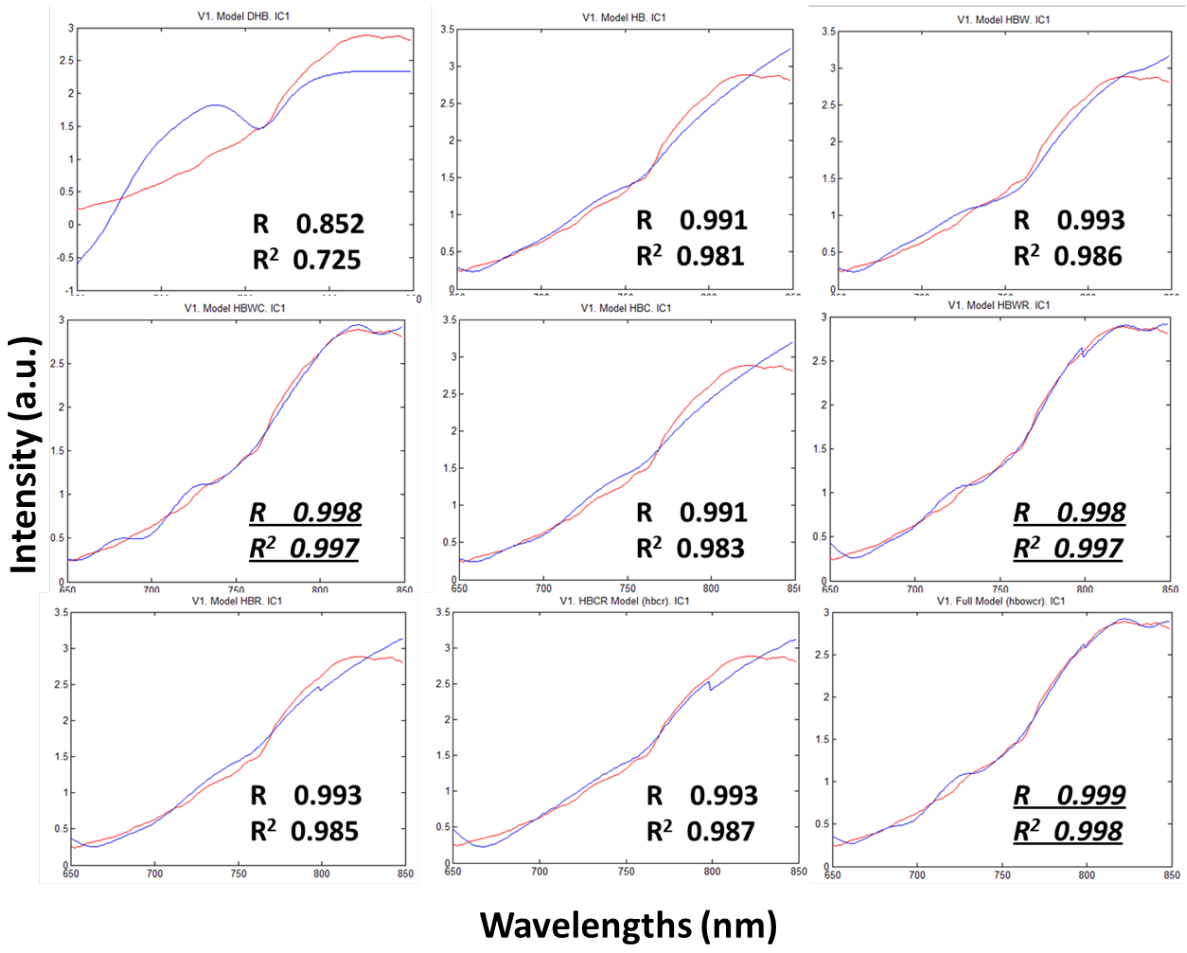

Figure 2.10: Nine combinations of various chromophores "visible" in near infrared region were fitted in the spectral component one (IC1). Correlation coefficient and the square of the CC are displayed on the graph.

mixing matrix. It was observed that across all the subjects there were always present two distinct shape spectra, as those plotted in Figure 2.5 (B) in red and blue. Figures 2.6 and 2.7 show the same spectral components plotted for the first four volunteers. To confirm that the shape of the spectrum (IC2) is a result of the experimental exercise, we tried to separate baseline data recorded during the same session, into independent components. Mixing matrix of those data contained spectral form of IC1 but not IC2.

We can speculate, based on fit coefficients and comparison of known spectra of oxy- and deoxy-haemoglobin with specrtal components of IC1 and IC2, that IC1 is mainly oxyhaemoglobin, whereas IC2 has both oxyhaemoglobin and deoxyhaemoglibin in approxiamtely equal parts.

Once the temporal components, and their counterpart spectral components, were identified, we further looked at the relationships between BOLD and optical data. Temporal components were correlated

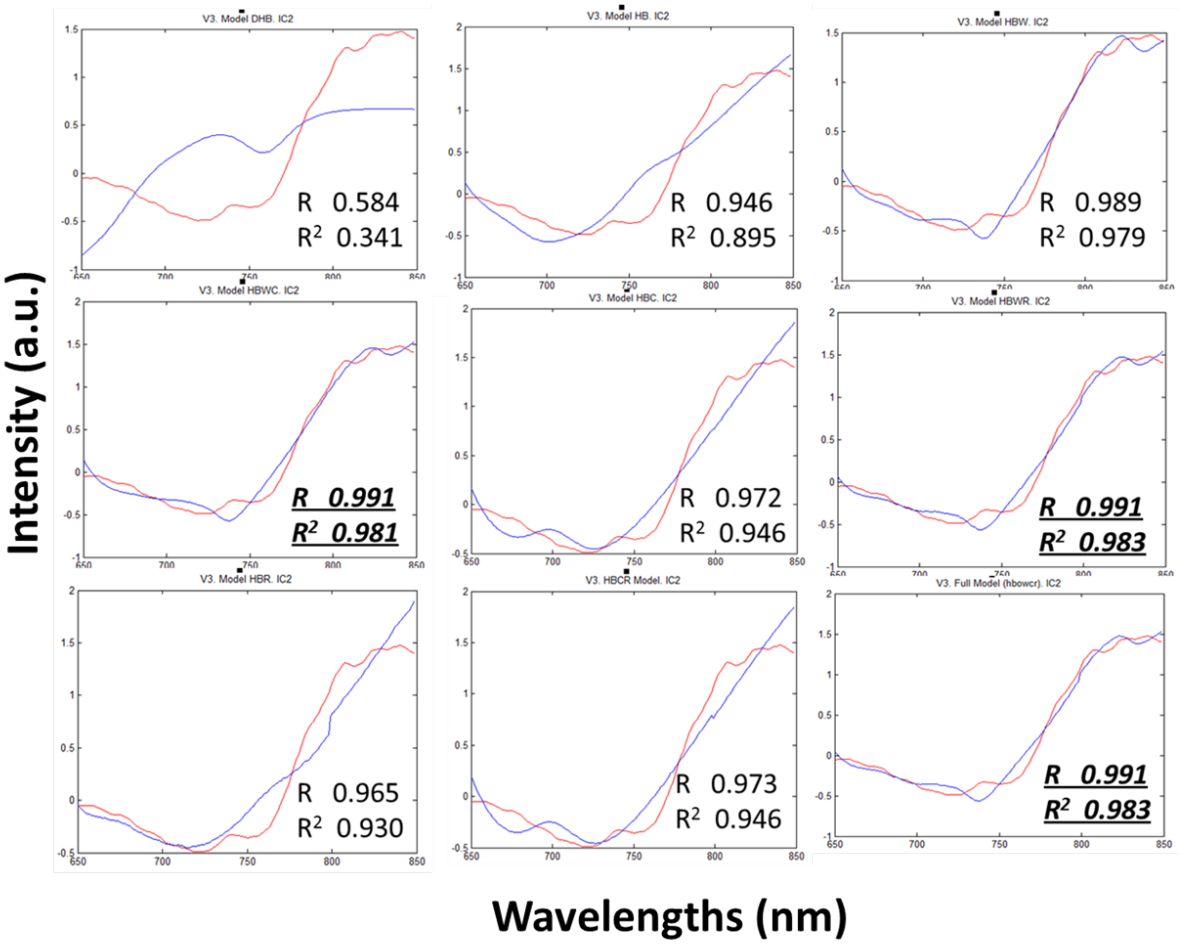

Figure 2.11: Fitting of the models into the spectral component of IC2. Correlation coefficients and R^2 are displayed on the graph.

with BOLD to observe spatial distribution of high correlation coefficients. We found that there were significant regions of the brain (for 7 out of 8 volunteers), where high correlation coefficients for the two components did not overlap spatially. Figure 2.8 shows an example of unique distributions of temporal correlates of the spectral components in the top panel. Although the locations were different, we could not conclude that the same unique locations were occupied by the components in all volunteers. In [77], we published volume averaged correlation coefficients for four types of methods of recovering relative haemoglobin concentrations. Comparing those correlation coefficients with the values obtained from correlating time courses of unknown mixtures with BOLD signal, it appears that the correlation coefficients are higher. Figure 2.9 shows correlation coefficients converted into maps of spatial distributions superimposed on the anatomical images. Selection of the threshold to separate the components was performed based on the visual examination of the strength of signal for each participant separately.

Once physiological processes behind the components are understood, such mapping would allow tracing of the anatomical origin of the signal.

Taking the other direction in Figure 2.4, shown by the red arrow path, led us to investigate the origin of the spectral mixtures. We assumed that chromophores visible in the near infrared region are known and their absorption spectra can be used to model the spectra. Nine models were fitted into the components (Figure 2.10 for IC1 and Figure 2.11 for IC2). As practically all the models were statistically significant, we evaluated the value of the model by the square of the correlation. For the IC1, three models produced similar correlation coefficients which may mean that they contain similar information. For the IC2, two models had the highest value of R^2.

Only the interval from 650 to 850 nm was fitted because only that part of the spectrum could be explained by the linear relationships. In Figure 2.12, we tried to fit a model into the entire range of wavelength, and it is obvious that the model does not describe the data that well as compared to the partial spectral fitting. One postulation would be that as wavelengths become longer the scattering increases. To minimize the residual, the differential path length factor (DPF) should be incorporated into modeling of the haemodynamic response. Thus, for future work, we intend to model a non-linear response using DPF available from literature.

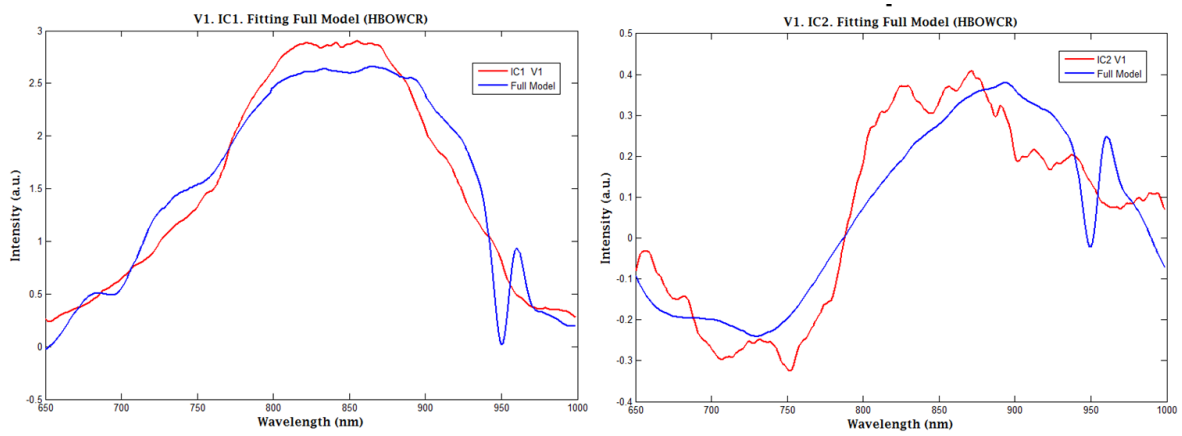

Figure 2.12: Fitting of the mixing coefficients for the full spectrum (650 - 1000 nm) for IC1 (left) and IC2 (right).

2.10 Conclusions

ICA have been extensively used to map haemodynamic response without prior knowledge of its time course. We applied FastICA method on the optical data collected from a breath hold experiment, and observed that there are two components which are associated with the increased CO_2 in blood. Correlation of time courses of those components with BOLD, produced ranges of CC, which were converted into spatial maps superimposed on the anatomical images. On the other hand, reduced spectral components

extracted from the mixing matrix were fitted into several models. It appears that DPF plays a role in goodness of the fitted models.

Chapter 3

Discussion and Conclusions

3.1 Discussion

In the first part of the thesis, cerebral response to breath hold experiment using broadband near-infrared set-up was recorded, and relative changes of HbO_2 and Hb were recovered using four different methods. The first method was based on two-wavelengths approach, as commercially manufactured NIR equipment is still largely driven by the limited number of spectral channels. The other three methods were based on different spectral fitting algorithms. Knowing the tissue differential pathlength factor (DPF), measured changes in optical attenuation were converted to the concentrations of Hb and HbO_2 in micromoles per litre. Recovered time courses of HbO_2 and Hb were compared to simultaneously acquired fMRI BOLD signal. The temporal course of $\Delta HbO_2(t)$ were always well correlated with the BOLD signal. However, temporal behaviour of $-\Delta Hb$ quantified using method 1 and 2 were qualitatively different from the time courses of the volume-average BOLD signals and from that of $-\Delta^3_{Hb}(t)$ and $-\Delta^4_{Hb}(t)$. The temporal signals obtained with method 3 and 4 were always consistent with the average time course of the BOLD signals. One should emphasize that methods 3 and 4 are essentially broadband ones as they used spectral derivatives of the absorbance changes over the range of approximately 258 wavelengths.

fMRI BOLD technique is routinely used to validate NIRS measurements in studies of cerebral hemodynamic responses to stimuli in humans. Thus, obtained temporal courses of optical signal were correlated with BOLD signal to determine which method would produce the highest correlation coefficients (CC). The highest group average of CC was obtained using first spectral derivative (Method 3) and the worst correlation was produced by the direct spectral absorbance fit (Method 2). Both Methods use GLM fitting algorithm but it was applied either to the absorbance change (Method 2) or to the spectral derivative of it (Methods 3). Difference in behavior of HbO_2 and Hb can be explained by the fact that during functional activation changes in the oxy- and deoxyhenoglobin concentrations take opposite directions due to the washout effect [109]. The increases in the HbO_2 concentration caused the entire absorbance spectrum to increase but this has a great effect in the longer wavelength, which is the half of our spectral band (wavelengths $> 800\ nm$). The decreases in the Hb concentration caused the opposite effect but preferentially in the short-wavelength part of the spectrum (wavelengths 700 - 800 nm).

Since the concentration of Hb in the brain is much smaller than that of HbO_2, relative changes in the former were also relatively small. The overall rise of the absorption across the spectral band (700 - 900 nm) was much stronger than the differences between the short- and the long-wavelength halves of the band. These differences in the effects of the oxy- and deoxyhemoglobin changes on the absorbance spectrum could result in a poor quantitation of $-\Delta Hb(t)$ by Methods 1 and 2 in the cases when signal distortions due to physiological or motion artifacts occurred. These distortions did not affect significantly $\Delta HbO_2(t)$ because of the larger amplitude of oxyhaemoglobin changes. However, the effect of $-\Delta Hb(t)$ and $\Delta HbO_2(t)$ on the spectral derivatives of the absorbance was better balanced than that on the absorbance itself because the differentiation eliminated the homogeneous changes across the spectrum and magnified the effect of the deoxyhemoglobin concentration changes due to the strong feature in the first- and second-order differential extinction spectra of deoxyhaemoglobin near 760 nm (see Figure 6 in [106].

The second differential extinction spectrum of the deoxyhemoglobin had even stronger feature near

760 nm than the first differential spectrum and, therefore, in terms of $-\Delta Hb(t)$ Method 4 could theoretically provide even better result than Method 3. However, since the second differential also magnified the spectral noise, the Method 3 provided the best correlation with BOLD. The two-wavelength Method 1 worked slightly better than the broadband Method 2 because the algorithm differences. The algorithm of Method 1 was based not on the fitting of the absorbance changes spectrum but rather on the solution of the linear system of equations for the absorption changes at 690 nm and 830 nm. At these two wavelengths the difference between the extinction spectra of Hb and HbO_2 were high and in particular at the 690 nm the HbO_2 extinction was minimal so that the effect of ΔHbO_2 changes at 690 nm was much smaller than the effect of Hb changes. However, both Method 3 and 4 outperformed Method 1 in terms of $\Delta Hb(t)$ quantitation.

In [95], the principal and the independent component analyses (PCA and ICA, respectively) were tested to remove the distorted haemodynamic signals measured by a two-wavelength system at 30 mm source-detector separations during breath holding. Both PCA and ICA produced better signals in cases of slight distortions, i.e. when typical exercise-synchronized increases in $\Delta HbO_2(t)$ and decreases in $\Delta Hb(t)$ were noticeable in non-cleaned data. Although these methods would not improve the behavior of off-phase signals such as the red curve (Method 2) in Figure 2(a), PCA and/or ICA could still be applied to the broadband data acquired at multiple source-detector distances to separate the contribution of the scalp from the cerebral signals. This should clarify whether the advanced signal processing techniques applied to the multi-distance data will be sufficient to resolve the problems of the two-wavelength method or the broadband approach is required to ensure the correct measurement of cerebral deoxyhemoglobin changes. On the other hand, our results show that our broadband Method 3 at least provides a single-channel alternative to PCA and ICA which require multi-channel measurements.

The second part of the thesis presents the results of a blind source separation method applied to the broadband data acquired at a single source-detector distance. ICA has been extensively used to map haemodynamic response without prior knowledge of its time course. The aim of this analysis was to determine if a statistical technique, applied to NIR data, has a potential to provide an additional information.

According to the schematic diagram (Figure 2.4, the right side), one part of the analysis had a purpose of correlating independent temporal components extracted from the NIR data with simultaneously acquired fMRI BOLD signal. Two temporal independent components (tICs) were identified in the optical data of each subject. Choice of the number of components is discussed below. Correlation of the temporal components with the respective fMRI BOLD signals at each voxel, produced the range of correlation coefficients for each component. Spatial distributions of the voxels with high correlation coefficients for each component (IC1 and IC2) were mapped on the MR anatomical images of the brain and compared to identify co-locations. It was observed that the spatial distribution of the voxels, in which independent components had high correlation with BOLD ($r = \pm 0.45$), appeared to non-overlap for seven out of eight subjects. The voxels with the CCs above the threshold were selected and converted into spatial maps for the co-registration of the regions of high correlation between ICs and BOLD. Although the clusters of high correlation were non-overlapping practically for all participants, no specific consistent pattern was determined. It remains to be seen whether tracing of those components contains

any physiologically meaningful information.

Left side of the 2.4 diagram displays spectral analysis of the temporal components IC1 and IC2 discussed above. One dimensional FastICA method was implemented to the same optical data sets collected from a breath hold experiment described in Part I of this thesis. For the first time, broadband NIR spectrum was analyzed using individual wavelengths as the discrete input channels to separate the data into independent temporal components with ICA. Spectral information of the temporal ICs contained in the A mixing matrix was utilized for the modeling physiological composition of the optical data collected during breath hold experiment (Figure 2.4, on the left).

One of the specificities of ICA is that the choice of the number of independent components (ICs) is decided based on either hypothesized number of signals available in the data, or dictated by the highest eigenvalues of the eigenvectors estimated during the pre-processing with principal component analysis. Although the NIRS data were processed to extract temporal components, selection of the number of the temporal ICs was performed through iteration and visual assessment of the spectral shapes on the A mixing matrix plot for each subject (Figure 2.5). Driven by the same beath hold cycle, the time evolution of chromophores concentration changes is expected to overlap. Therefore, visual determination of the independence of two time courses is practically impossible. Since, the mixing matrix contains unique spectral shapes of the respective temporal components, by routinely observing its plot, selection of temporal components was established as two original time evolutions of unknown combinations of chromophores. The same two visually distinct spectral shapes in A mixing matrices were evident for all subjects ($n = 16$) (Figures 2.6 and 2.7). However, whether the two components were the result of the functional activation such as breath hold exercise or a property of the resting state was determined through the comparison of experimental results with the baseline condition obtained on the same subject prior just before the procedure. Presence of the IC1 and not IC2 indicated that the spectral component two is induced by the changes in the functional state.

Spectral components extracted with FastICA do not represent individual time series of pure chromophores concentration changes such as HbO_2 and Hb. It was hypothesized that each component is an interplay of the two major chromophores changes at different moments of the functional activation. Identifying the origin of the components via fitting of various models into the spectral part of the tICs was the goal of general linear modelling (GLM). On one hand, spectral analysis of the components had a point of evaluating what would be the best linear model to describe the shape of the components. This was achieved based on the comparison of R^2 for the models discussed previously. On the other hand, assessment of the fit coefficients for each chromophore would provide an idea of their individual contribution, and hence, give an indication of the correspondence of the spectral component to a physiological state.

Since, attenuation dominates in the first half of the NIR spectrum (650 to 850 nm), eight linear combination of extinction coefficients of various chromophores were fitted only into that part of the spectral components. Figures 2.10 and 2.11 demonstrate that for this range of wavelenths linear fit of the data worked very well. However, in the region of longer wavelengths, the water absorption dominates and the mean free path of photons in biological tissue also increases. Figure 2.12 show that fitting a linear model of attenuation coefficients did not describe optical data fully. Hence, including scattering factor,

differential pathlength factor, in to the model would certainly improve the goodness of the fit. Also, inclusion of other chromophore such as water, or a low concentration chromophore such as cytochrome-c-oxidase appears to improve the overall fitting. Whether cytochrome itself significantly contributes to the fitting remains to be statistically determined. However, with some degree of certainty, it can be ascertained that fitting of water attenuation spectrum into the model was crucial for obtaining high values of R^2.

Numerical evaluation of the contribution of individual chromophore to a model was assessed based on the values of regression coefficients. For each participant, the ratio of the values of regression coefficients for spectral IC1 and IC2 remained constant, i.e. for IC1, contribution by the oxyhaemoglobin was above 80 per cent; for IC2, contribution by oxy- and deoxyhemoglobin was approximately equal. In the context of the breath hold experiment, it was hypothesized that the spectral component 1 represents the change in the blood volume, whereas the spectral component 2 might correspond to the washout effect.

To our best knowledge, there were no reports of usage of the A mixing matrix for the purposes of selection of number of independent components, and/or evaluation of the spectral features of the NIRS data. Thus, analysis of NIR signal presented in this thesis has its novelty and might have a potential to provide new insights into the physiological mechanisms of the brain haemodynamics.

3.2 Conclusions

Broadband NIRS is not just "much more wavelengths" but rather a qualitatively different modality which enables implementation of various signal processing techniques that can only be achieved with continuous spectrum of wavelengths. In support of that correlation analysis of NIRS and BOLD time series revealed that broadband NIRS techniques using spectral derivative algorithms, especially first derivative of the absorbance spectrum, had higher correlation coefficients as compared to the multi-wavelength methods.

Also, application of ICA to broadband NIRS data can provide temporal and spectral information of the available independent components using a single source detector configuration probe. Linear fitting of spectral components of the A mixing matrix has its merits in terms of revealing spectral composition and functional state of underlying physiological processes. In the context of breath hold experiment, it can be described as follows: CO_2 causes vasodilation and consequent increase in cerebral blood flow, which, in turn, causes washing out of deoxyhaemoglobin from the capillary bed.

3.3 Future Work

In future work, to address issues of extracerebral interference, application of the independent and principal component analyses to the broadband data acquired at multiple source-detector distances might be implemented. This should evaluate whether the advanced signal processing techniques applied to the multi-distance data will be sufficient to resolve the problems of the two-wavelength method or the broadband approach is required to ensure the correct measurement of cerebral deoxyhemoglobin changes.

Correlational analysis of temporal independent components with BOLD signal could assist in map-

ping functional activation to the anatomical origin of the signal. That part of the work was not pursued in this thesis but deserves further investigation. Furthermore, evaluation of the ICA analysis of broadband NIRS in response to neuronal activation such as motor task or visual stimulation can be undertaken to observe how the nature of the spectral components depends on the functional stimulation and the origin of a stimulus. Development of broadband NIR signal processing methods can reveal new information about the functional state of the brain and help clinicians in monitoring of cerebral haemodynamic response.

References

[1] G. Jasdzewski, G. Strangman, J. Wagner, K. Kwong, R. Poldrack, and D. Boas, "Differences in the hemodynamic response to event-related motor and visual paradigms as measured by near-infrared spectroscopy," *NeuroImage*, vol. 20, no. 1, pp. 479–488, 2003. cited By (since 1996) 80.

[2] G. Gratton and P. Corballis, "Removing the heart from the brain: Compensation for the pulse artifact in the photon migration signal," *Psychophysiology*, vol. 32, no. 3, pp. 292–299, 1995. cited By (since 1996) 69.

[3] B. Chance, E. Anday, S. Nioka, S. Zhou, L. Hong, K. Worden, C. Li, T. Murray, Y. Ovetsky, D. Pidiklti, and R. Thomas, "A novel method for fast imaging of brain function, non-invasively, with light," *Optics Express*, vol. 2, no. 10, pp. 411–423, 1998. cited By (since 1996) 156.

[4] Y. Hoshi, S.-J. Chen, and M. Tamura, "Spatiotemporal imaging of human brain activity by functional near-infrared spectroscopy," *American Laboratory*, vol. 33, no. 20, pp. 35–36+38, 2001. cited By (since 1996) 9.

[5] T. Muehlemann, D. Haensse, and M. Wolf, "Wireless miniaturized in-vivo near infrared imaging," *Optics Express*, vol. 16, no. 14, pp. 10323–10330, 2008. cited By (since 1996) 8.

[6] G. Csibra, J. Henty, A. Volein, C. Elwell, L. Tucker, J. Meek, and M. Johnson, "Near infrared spectroscopy reveals neural activation during face perception in infants and adults," *Journal of Pediatric Neurology*, vol. 2, pp. 85 – 89, 2004// 2004. exported from refbase (http://www.bibliography.ceu.hu/show.php?record=4843), last updated on Thu, 16 Jul 2009 11:29:28 +0200.

[7] H. Negoro, M. Sawada, J. Iida, T. Ota, S. Tanaka, and T. Kishimoto, "Prefrontal dysfunction in attention-deficit/hyperactivity disorder as measured by near-infrared spectroscopy," *Child Psychiatry and Human Development*, vol. 41, no. 2, pp. 193–203, 2010. cited By (since 1996) 2.

[8] V. Quaresima, R. Lepanto, and M. Ferrari, "The use of near infrared spectroscopy in sports medicine," *Journal of Sports Medicine and Physical Fitness*, vol. 43, no. 1, pp. 1–13, 2003. cited By (since 1996) 63.

[9] K. Izzetoglu, S. Bunce, B. Onaral, K. Pourrezaei, and B. Chance, "Functional optical brain imaging using near-infrared during cognitive tasks," *International Journal of Human-Computer Interaction*, vol. 17, no. 2, pp. 211–227, 2004. cited By (since 1996) 33.

[10] D. A. Boas, D. H. Brooks, E. L. Miller, C. A. DiMarzio, M. Kilmer, and R. J. Gaudette, "Imaging the body with diffuse optical tomography," *Signal Processing Magazine, IEEE*, vol. 18, no. 6;, pp. 57–75, 2001. ID: 1.

[11] Y. Hoshi, "Functional near-infrared optical imaging: Utility and limitations in human brain mapping," *Psychophysiology*, vol. 40, no. 4, pp. 511–520, 2003. cited By (since 1996) 122.

[12] D. T. Delpy, M. Cope, P. Van Der Zee, S. Arridge, S. Wray, and J. Wyatt, "Estimation of optical pathlength through tissue from direct time of flight measurement.," *Physics in Medicine and Biology*, vol. 33, no. 12, pp. 1433–1442, 1988.

[13] M. Patterson, B. Chance, and B. Wilson, "Time resolved reflectance and transmittance for the non-invasive measurement of tissue optical properties," *Appl. Opt.*, vol. 28, pp. 2331–2336, Jun 1989.

[14] Chance, B., Leigh, J. S., Miyake, H., Smith, D. S., Nioka, S., Greenfeld, R., Finander, M., Kaufmann, K., Levy, W., Young, M., Cohen, P., Yoshioka, H., and Boretsky, R., "Comparison of time-resolved and -unresolved measurements of deoxyhemoglobin in brain," *Proceedings of the National Academy of Sciences of the United States of America*, vol. 85, no. 14, pp. 4971–4975, 1988.

[15] B. Chance, S. Nioka, J. Kent, K. McCully, M. Fountain, R. Greenfeld, and G. Holtom, "Time-resolved spectroscopy of hemoglobin and myoglobin in resting and ischemic muscle," *Analytical Biochemistry*, vol. 174, no. 2, pp. 698–707, 1988. cited By (since 1996) 153.

[16] E. Gratton, V. Toronov, U. Wolf, M. Wolf, and A. Webb, "Measurement of brain activity by near-infrared light," *Journal of Biomedical Optics*, vol. 10, no. 1, pp. 1–13, 2005. cited By (since 1996) 22.

[17] E. Gratton, W. W. Mantulin, M. J. vandeVen, M. B. Fishkin, J. B.and Maris, and B. Chance, "The possibility of a near-infrared optical imaging system using frequency-domain methods," *Proceedings of the Third International Conference on Peace through Mind/Brain Science (Hamamatsu, Hamamatsu City, Japan, 1990*, pp. 183–189, 1990.

[18] I.-Y. Son and B. Yazici, "Near infrared imaging and spectroscopy for brain activity monitoring," *NATO Security through Science Series A: Chemistry and Biology*, pp. 341–372, 2006. cited By (since 1996) 0.

[19] F. Jobsis, "Noninvasive, infrared monitoring of cerebral and myocardial oxygen sufficiency and circulatory parameters," *Science*, vol. 198, no. 4323, pp. 1264–1267, 1977. cited By (since 1996) 1213.

[20] A. Villringer, J. Planck, C. Hock, L. Schleinkofer, and U. Dirnagl, "Near infrared spectroscopy (nirs): A new tool to study hemodynamic changes during activation of brain function in human adults," *Neuroscience Letters*, vol. 154, no. 1-2, pp. 101 – 104, 1993.

[21] A. Bozkurt, A. Rosen, H. Rosen, and B. Onaral, "A portable near infrared spectroscopy system for bedside monitoring of newborn brain," *BioMedical Engineering Online*, vol. 4, 2005. cited By (since 1996) 22.

[22] L. V. Wang and H.-i. Wu, *Biomedical Optics - Principles and Imaging*. Wiley-Interscience, 2007.

[23] F. L. Pedrotti, L. Pedrotti, and L. Pedrotti, *Introduction to Optics (3rd Edition)*. Benjamin Cummings, 3 ed., Apr. 2006.

[24] S. Arridge, "Optical tomography in medical imaging," *Inverse Problems*, vol. 15, no. 2, pp. R41–R49, 1999. cited By (since 1996) 925.

[25] M. Hiraoka, M. Firbank, M. Essenpreis, M. Cope, S. Arridge, P. Van Der Zee, and D. Delpy, "A monte carlo investigation of optical pathlength in inhomogeneous tissue and its application to near-infrared spectroscopy," *Physics in Medicine and Biology*, vol. 38, no. 12, pp. 1859–1876, 1993. cited By (since 1996) 162.

[26] R. Groenhuis, H. Ferwerda, and J. Ten Bosch, "Scattering and absorption of turbid materials determined from reflection measurements. 1: Theory.," *Applied Optics*, vol. 22, no. 16, pp. 2456–2462, 1983. cited By (since 1996) 237.

[27] E. Aydin, C. De Oliveira, and A. Goddard, "A comparison between transport and diffusion calculations using a finite element-spherical harmonics radiation transport method," *Medical Physics*, vol. 29, no. 9, pp. 2013–2023, 2002. cited By (since 1996) 32.

[28] A. Sassaroli and S. Fantini, "Comment on the modified beer-lambert law for scattering media," *Physics in Medicine and Biology*, vol. 49, no. 14, pp. N255–N257, 2004. cited By (since 1996) 22.

[29] M. Cope and D. Delpy, "System for long-term measurement of cerebral blood and tissue oxygenation on newborn infants by near infra-red transillumination," *Medical and Biological Engineering and Computing*, vol. 26, no. 3, pp. 289–294, 1988. cited By (since 1996) 312.

[30] E. O. R. Reynolds, J. S. Wyatt, D. Azzopardi, D. T. Delpy, E. B. Cady, M. Cope, , and S. Wray, "New non-invasive methods for assessing brain oxygenation and hemodynamics," *British Medical Bulletin*, vol. 44, p. 10521075, 1988.

[31] H. Obrig and A. Villringer, "Beyond the visible - imaging the human brain with light," *Journal of Cerebral Blood Flow and Metabolism*, vol. 23, no. 1, pp. 1–18, 2003. cited By (since 1996) 220.

[32] H. Obrig, R. Wenzel, M. Kohl, S. Horst, P. Wobst, J. Steinbrink, F. Thomas, and A. Villringer, "Near-infrared spectroscopy: does it function in functional activation studies of the adult brain?," *International Journal of Psychophysiology*, vol. 35, no. 2-3, pp. 125 – 142, 2000.

[33] H. R. Heekeren, M. Kohl, H. Obrig, R. Wenzel, W. Pannwitz, S. Matcher, C. Dirnagl, U.and Cooper, and A. Villranger, "Noninvasive assessment of changes in cytochrom-c-oxidase oxidation in human subjects during visual stimulation.," *Journal of Cerebral Blood Flow and Metabolism*, vol. 19, p. 592603, 1999.

[34] M. Kohl, C. Nolte, H. Heekeren, S. Horst, U. Scholz, H. Obrig, and A. Villringer, "Changes in cytochrome-oxidase oxidation in the occipital cortex during visual stimulation: Improvement in sensitivity by the determination of the wavelength dependence of the differential pathlength factor," vol. 3194, pp. 18–27, 1997. cited By (since 1996) 0.

[35] K. Uludag, M. Kohl, J. Steinbrink, H. Obrig, and A. Villringer, "Cross talk in the lambert-beer calculation for near-infrared wavelengths estimated by monte carlo simulations," *Journal of Biomedical Optics*, vol. 7, no. 1, pp. 51–59, 2002. cited By (since 1996) 63.

[36] M. Cope, *The development of a near infrared spectroscopy system and its application for non invasive monitoring of cerebral blood and tissue oxygenation in the newborn infant.* PhD thesis, 1991.

[37] R. Bonner, R. Nossal, S. Havlin, and G. Weiss, "Model for photon migration in turbid biological media.," *Journal of the Optical Society of America. A, Optics and image science*, vol. 4, no. 3, pp. 423–432, 1987. cited By (since 1996) 152.

[38] A. Villringer and B. Chance, "Non-invasive optical spectroscopy and imaging of human brain function," *Trends in Neurosciences*, vol. 20, no. 10, pp. 435–442, 1997. cited By (since 1996) 502.

[39] E. Okada, M. Firbank, M. Schweiger, S. Arridge, M. Cope, and D. Delpy, "Theoretical and experimental investigation of near-infrared light propagation in a model of the adult head," *Applied Optics*, vol. 36, no. 1, pp. 21–31, 1997. cited By (since 1996) 230.

[40] M. Firbank, E. Okada, and D. Delpy, "A theoretical study of the signal contribution of regions of the adult head to near-infrared spectroscopy studies of visual evoked responses," *NeuroImage*, vol. 8, no. 1, pp. 69–78, 1998. cited By (since 1996) 107.

[41] N. Okui and E. Okada, "Wavelength dependence of crosstalk in dual-wavelength measurement of oxy- and deoxy-hemoglobin," *Journal of Biomedical Optics*, vol. 10, no. 1, pp. 1–8, 2005. cited By (since 1996) 7.

[42] O. Pucci, V. Toronov, and K. St. Lawrence, "Measurement of the optical properties of a two-layer model of the human head using broadband near-infrared spectroscopy," *Applied Optics*, vol. 49, no. 32, pp. 6324–6332, 2010. cited By (since 1996) 0.

[43] J. Thompson, M. Peterson, and R. Freeman, "Single-neuron activity and tissue oxygenation in the cerebral cortex," *Science*, vol. 299, no. 5609, pp. 1070–1073, 2003. cited By (since 1996) 134.

[44] J. E. W. Mayhew, S. Askew, Y. Zheng, J. Porrill, G. W. M. Westby, P. Redgrave, D. M. Rector, and R. M. Harper, "Cerebral vasomotion: A 0.1-hz oscillation in reflected light imaging of neural activity," *NeuroImage*, vol. 4, no. 3, pp. 183 – 193, 1996.

[45] C. Elwell, R. Springett, E. Hillman, and D. Delpy, "Oscillations in cerebral haemodynamics: Implications for functional activation studies," *Advances in Experimental Medicine and Biology*, vol. 471, pp. 57–65, 2000. cited By (since 1996) 39.

[46] A. Malliani, M. Pagani, and F. Lombardi, "Physiology and clinical implications of variability of cardiovascular parameters with focus on heart rate and blood pressure," *American Journal of Cardiology*, vol. 73, no. 10, pp. C3–C9, 1994. cited By (since 1996) 73.

[47] N. Lundberg, "Continuous recording and control of ventricular fluid pressure in neurosurgical practice.," *Acta psychiatrica Scandinavica. Supplementum*, vol. 36, no. 149, pp. 1–193, 1960. cited By (since 1996) 259.

[48] J. Mayhew, Y. Zheng, Y. Hou, B. Vuksanovic, J. Berwick, S. Askew, and P. Coffey, "Spectroscopic analysis of changes in remitted illumination: The response to increased neural activity in brain," *NeuroImage*, vol. 10, no. 3 I, pp. 304–326, 1999. cited By (since 1996) 79.

[49] R. L. Savoy, M. E. Ravicz, and R. Gollub, "The psychophysiological laboratory in the magnet: stimulus delivery, response recording, and safety," *In C. T. W. Moonen and P. A. Bandettini (Eds.), Functional MRI, Berlin: Springer*, p. 347365, 1999.

[50] P. Bandettini, "The temporal resolution of mri," *In: Functional MRI (ed. C.T.W. Moonen and P. Bandettini), Springer- Verlag, Mauer, Germany*, p. 205220, 1999.

[51] C. Moonen, P. Van Zijl, J. Frank, D. Le Bihan, and E. Becker, "Functional magnetic resonance imaging in medicine and physiology," *Science*, vol. 250, no. 4977, pp. 53–61, 1990. cited By (since 1996) 60.

[52] C. S. J. Springer, C. S. Patlak, I. Palyka, and W. Huang, "Principles of susceptibility contrast-based functional mri: The sign of the functional mri response," *in Functional MRI, C. T. W. Moonen and P. A. Bandettini, Eds. New York: Springer*, pp. 91 – 102, 2000.

[53] S. Fox, *Human physiology*. McGraw-Hill, 2004.

[54] L. Pauling and C. Coryell, "The magnetic properties and structure of hemoglobin," *The Proceedings of the National Academy of Sciences Online (U.S.)*, no. 22, pp. 210 – 216, 1936.

[55] S. Ogawa, T. Lee, A. Kay, and D. Tank, "Brain magnetic resonance imaging with contrast dependent on blood oxygenation," *Proceedings of the National Academy of Sciences of the United States of America*, vol. 87, no. 24, pp. 9868–9872, 1990. cited By (since 1996) 1863.

[56] S. Ogawa, R. Menon, D. Tank, S.-G. Kim, H. Merkle, J. Ellermann, and K. Ugurbil, "Functional brain mapping by blood oxygenation level-dependent contrast magnetic resonance imaging. a comparison of signal characteristics with a biophysical model," *Biophysical Journal*, vol. 64, no. 3, pp. 803–812, 1993. cited By (since 1996) 745.

[57] K. Kwong, "Functional magnetic resonance imaging with echo planar imaging," *Magnetic Resonance Quarterly*, vol. 11, no. 1, pp. 1–20, 1995. cited By (since 1996) 159.

[58] P. T. Callaghan, *Principles of nuclear magnetic resonance microscopy*. Oxford Science Publications, Oxford University Press, 1993.

[59] S. Ogawa, T. Lee, A. Kay, and D. Tank, "Brain magnetic resonance imaging with contrast dependent on blood oxygenation," *Proceedings of the National Academy of Sciences of the United States of America*, vol. 87, no. 24, pp. 9868–9872, 1990. cited By (since 1996) 1863.

[60] G. Glover, "Deconvolution of impulse response in event-related bold fmri," *NeuroImage*, vol. 9, no. 4, pp. 416–429, 1999. cited By (since 1996) 418.

[61] J. Martindale, J. Mayhew, J. Berwick, M. Jones, C. Martin, D. Johnston, P. Redgrave, and Y. Zheng, "The hemodynamic impulse response to a single neural event," *Journal of Cerebral Blood Flow and Metabolism*, vol. 23, no. 5, pp. 546–555, 2003. cited By (since 1996) 60.

[62] Y. Yang, W. Engelien, H. Pan, D. Xu, S.and Silbersweig, and E. Stern, "A cbf-based event-related brain activation paradigm: Characterization of impulse-response function and comparison to bold," *NeuroImage*, vol. 12, no. 3, pp. 287 – 297, 2000.

[63] Y. Pu, H.-L. Liu, A. Spinks, S. Mahankali, C.-M. Xiong, J. andi Feng, H. Tan, P. Fox, and J. Gao, "Cerebral hemodynamic response in chinese (first) and english (second) language processing revealed by event-related functional mri," *Magnetic resonance imaging*, vol. 19, no. 5, pp. 643–647, 2001.

[64] M. Mohamed, D. Yousem, A. Tekes, N. Browner, and V. Calhoun, "Correlation between the amplitude of cortical activation and reaction time: A functional mri study," *American Journal of Roentgenology*, vol. 183, no. 3, pp. 759–765, 2004. cited By (since 1996) 11.

[65] P. Jezzard, P. Matthews, and S. Smith, *Functional MRI: an introduction to methods*. Oxford medical publications, Oxford University Press, 2001.

[66] K. J. Friston, S. Williams, R. Howard, R. S. J. Frackowiak, and R. Turner, "Movement-related effects in fmri time-series," *Magnetic Resonance in Medicine*, vol. 35, no. 3, pp. 346–355, 1996.

[67] R. Frostig, E. Lieke, D. Ts'o, and A. Grinvald, "Cortical functional architecture and local coupling between neuronal activity and the microcirculation revealed by in vivo high-resolution optical imaging of intrinsic signals," *Proceedings of the National Academy of Sciences of the United States of America*, vol. 87, no. 16, pp. 6082–6086, 1990. cited By (since 1996) 455.

[68] D. Moore and G. McCabe, *Introduction to the Practice of Statistics Chapters 14-17*. W. H. Freeman, 2005.

[69] N. Logothetis and B. Wandell, "Interpreting the bold signal," *Annual Review of Physiology*, vol. 66, pp. 735–769, 2004. cited By (since 1996) 358.

[70] P. Prasad, *Introduction to biophotonics*. Wiley-Interscience, 2003.

[71] A. Kleinschmidt, H. Obrig, M. Requardt, K.-D. Merboldt, U. Dirnagl, A. Villringer, and J. Frahm, "Simultaneous recording of cerebral blood oxygenation changes during human brain activation by magnetic resonance imaging and near-infrared spectroscopy," *Journal of Cerebral Blood Flow and Metabolism*, vol. 16, no. 5, pp. 817–826, 1996. cited By (since 1996) 197.

[72] D. Mehagnoul-Schipper, B. Van Der Kallen, W. Colier, M. Van Der Sluijs, L. Van Erning, H. Thijssen, B. Oeseburg, W. Hoefnagels, and R. Jansen, "Simultaneous measurements of cerebral oxygenation changes during brain activation by near-infrared spectroscopy and functional magnetic resonance imaging in healthy young and elderly subjects," *Human Brain Mapping*, vol. 16, no. 1, pp. 14–23, 2002. cited By (since 1996) 85.

[73] V. Toronov, A. Webb, J. Choi, M. Wolf, A. Michalos, E. Gratton, and D. Hueber, "Investigation of human brain hemodynamics by simultaneous near-infrared spectroscopy and functional magnetic resonance imaging," *Medical Physics*, vol. 28, no. 4, pp. 521–527, 2001. cited By (since 1996) 135.

[74] G. Strangman, J. Culver, J. Thompson, and D. Boas, "A quantitative comparison of simultaneous bold fmri and nirs recordings during functional brain activation," *NeuroImage*, vol. 17, no. 2, pp. 719–731, 2002. cited By (since 1996) 206.

[75] V. Toronov, A. Webb, J. Choi, M. Wolf, L. Safonova, U. Wolf, and E. Gratton, "Study of local cerebral hemodynamics by frequency-domain near-infrared spectroscopy and correlation with simultaneously acquired functional magnetic resonance imaging," *Optics Express*, vol. 9, no. 8, pp. 417–427, 2001. cited By (since 1996) 37.

[76] V. Toronov, S. Walker, R. Gupta, J. Choi, E. Gratton, D. Hueber, and A. Webb, "The roles of changes in deoxyhemoglobin concentration and regional cerebral blood volume in the fmri bold signal," *NeuroImage*, vol. 19, no. 4, pp. 1521–1531, 2003. cited By (since 1996) 52.

[77] I. Schelkanova and V. Toronov, "Optimal quantitation of the cerebral hemodynamic response in functional nearinfrared spectroscopy," *Optics Express*, vol. 18, no. 18, pp. 19386–19395, 2010. cited By (since 1996) 1.

[78] A. Hyvarinen, J. Karhunen, and E. Oja, *Independent component analysis*. Adaptive and learning systems for signal processing, communications, and control, J. Wiley, 2001.

[79] J. Stone, *Independent component analysis: a tutorial introduction*. Bradford Books, MIT Press, 2004.

[80] P. Comon, "Independent component analysis, a new concept?," *Signal Processing*, vol. 36, no. 3, pp. 287–314, 1994. cited By (since 1996) 2889.

[81] C. Jutten and J. Herault, "Blind separation of sources, part i: An adaptive algorithm based on neuromimetic architecture," *Signal Processing*, vol. 24, no. 1, pp. 1–10, 1991. cited By (since 1996) 1004.

[82] P. Huber, "Projection pursuit," *The Annals of Statistics*, vol. 13, no. 2, pp. pp. 435–475, 1985.

[83] T. Cover and J. Thomas, *Elements of information theory*. Wiley Series in Telecommunications and Signal Processing, Wiley-Interscience, 2006.

[84] A. Papoulis, *Probability, random variables, and stochastic processes*. McGraw-Hill series in electrical engineering: Communications and signal processing, McGraw-Hill, 1991.

[85] N. Kampen, *Stochastic processes in physics and chemistry*. North-Holland personal library, Elsevier, 2007.

[86] A. Hyvarinen, "Fast and robust fixed-point algorithms for independent component analysis," 1999.

[87] A. Hyvarinen and E. Oja, "A fast fixed-point algorithm for independent component analysis," *Neural Computation*, vol. 9, pp. 1483–1492, 1997.

[88] A. Hyvarinen, H. Gvert, J. Hurri, and J. Srel, "Fast independent component analysis for matlab 7.x and 6.x," 2005.

[89] S. Kohno, I. Miyai, A. Seiyama, I. Oda, A. Ishikawa, S. Tsuneishi, T. Amita, and K. Shimizu, "Removal of the skin blood flow artifact in functional near-infrared spectroscopic imaging data through independent component analysis," vol. 12, no. 6, p. 062111, 2007.

[90] G. D. Brown, S. Yamada, and T. J. Sejnowski, "Independent component analysis at the neural cocktail party," *Trends in Neurosciences*, vol. 24, no. 1, pp. 54 – 63, 2001.

[91] A. V. Medvedev, J. Kainerstorfer, S. V. Borisov, R. L. Barbour, and J. VanMeter, "Event-related fast optical signal in a rapid object recognition task: Improving detection by the independent component analysis," *Brain Research*, vol. 1236, pp. 145 – 158, 2008.

[92] T. Katura, H. Sato, Y. Fuchino, T. Yoshida, H. Atsumori, M. Kiguchi, A. Maki, M. Abe, and N. Tanaka, "Extracting task-related activation components from optical topography measurement using independent components analysis," vol. 13, no. 5, p. 054008, 2008.

[93] M. McKeown, T. Jung, S. Makeig, and T. Sejnowski, "Spatially independent activity patterns in functional mri data during the stroop color-namingtask," *Proc Natl Acad Sci U S A*, vol. 95, no. 3, pp. 803 – 810, 1998.

[94] M. S. Bartlett, *Face Image Analysis by Unsupervised Learning*. International Series on Engineering and Computer Science, Boston., Kluwer Academic Publishers, 2001.

[95] J. Virtanen, T. Noponen, and P. Merilinen, "Comparison of principal and independent component analysis in removing extracerebral interference from near-infrared spectroscopy signals," vol. 14, no. 5, p. 054032, 2009.

[96] M. A. Quigley, V. M. Haughton, J. Carew, D. Cordes, C. H. Moritz, and M. E. Meyerand, "Comparison of independent component analysis and conventional hypothesis-driven analysis for clinical functional mr image processing," *AJNR Am J Neuroradiol*, vol. 23, no. 1, pp. 49–58, 2002.

[97] H. Zhang, L. Duan, Y.-J. Zhang, C.-M. Lu, H. Liu, and C.-Z. Zhu, "Test-retest assessment of independent component analysis-derived resting-state functional connectivity based on functional near-infrared spectroscopy," *NeuroImage*, vol. 55, no. 2, pp. 607 – 615, 2011.

[98] A. Field, *Discovering statistics using SPSS: (and sex and drugs and rock 'n' roll)*. Introducing Statistical Methods Series, SAGE, 2009.

[99] A. Gibson and H. Dehghani, "Diffuse optical imaging," *Philosophical Transactions of the Royal Society A: Mathematical, Physical and Engineering Sciences*, vol. 367, no. 1900, pp. 3055–3072, 2009.

[100] S. Perrey, "Non-invasive nir spectroscopy of human brain function during exercise," *Methods*, vol. 45, no. 4, pp. 289 – 299, 2008. Neuroimaging in the sports sciences.

[101] M. Calderon-Arnulphi, A. Alaraj, and K. Slavin, "Near infrared technology in neuroscience: past, present and future," *Neurological Research*, vol. 31, no. 6, 2009.

[102] G. Pfurtscheller, G. Bauernfeind, S. C. Wriessnegger, and C. Neuper, "Focal frontal (de)oxyhemoglobin responses during simple arithmetic," *International Journal of Psychophysiology*, vol. 76, no. 3, pp. 186 – 192, 2010.

[103] C. Fedorow and H. Grocott, "Cerebral monitoring to optimize outcomes after cardiac surgery," *Current Opinion in Anaesthesiology*, vol. 23, no. 1, pp. 89–94, 2010. cited By (since 1996) 8.

[104] M. Martin, M. Wabuyele, M. Panjehpour, B. Overholt, R. DeNovo, S. Kennel, G. Cunningham, and T. Vo-Dinh, "An aotf-based dual-modality hyperspectral imaging system (dmhsi) capable of simultaneous fluorescence and reflectance imaging," *Medical Engineering and Physics*, vol. 28, no. 2, pp. 149 – 155, 2006.

[105] S. C. Gebhart, R. C. Thompson, and A. Mahadevan-Jansen, "Liquid-crystal tunable filter spectral imaging for brain tumor demarcation," *Appl. Opt.*, vol. 46, pp. 1896–1910, Apr 2007.

[106] S. Matcher, M. Cope, and D. Delpy, "Use of the water absorption spectrum to quantify tissue chromophore concentration changes in near-infrared spectroscopy.," *Physics in Medicine and Biology*, vol. 39, no. 1, pp. 177–196, 1994.

[107] E. Cooper, C. Elwell, J. Meek, J. Matcher, S. J.and Wyatt, M. Cope, and D. Delpy, "The noninvasive measurement of absolute cerebral deoxy-hemoglobin concentration and mean optical pathlength in the neonatal brain by second derivative near infrared spectroscopy.," *Pediatr. Res.*, vol. 39, no. 1, pp. 32 – 38, 1996.

[108] B. J. MacIntosh, L. Klassen, and R. S. Menon, "Transient hemodynamics during a breath hold challenge in a two part functional imaging study with simultaneous near-infrared spectroscopy in adult humans," *NeuroImage*, vol. 20, no. 2, pp. 1246 – 1252, 2003.

[109] L. P. Safonova, A. Michalos, U. Wolf, M. Wolf, D. M. Hueber, J. H. Choi, R. Gupta, C. Polzonetti, W. W. Mantulin, and E. Gratton, "Age-correlated changes in cerebral hemodynamics assessed by near-infrared spectroscopy," *Archives of Gerontology and Geriatrics*, vol. 39, no. 3, pp. 207 – 225, 2004.

[110] L. M. Klassen, B. J. MacIntosh, and R. S. Menon, "Influence of hypoxia on wavelength dependence of differential pathlength and near-infrared quantification.," *Physics in Medicine and Biology*, vol. 47, no. 9, pp. 1573–1589, 2002.

[111] B. Cerf-Ducastel and C. Murphy, "Afni.fmri brain activation in response to odors is reduced in primary olfactory areas of elderly subjects," *Brain Research*, vol. 986, no. 1-2, pp. 39 – 53, 2003.

[112] A. Sassaroli, B. deB. Frederick, Y. Tong, P. F. Renshaw, and S. Fantini, "Spatially weighted bold signal for comparison of functional magnetic resonance imaging and near-infrared imaging of the brain," *NeuroImage*, vol. 33, no. 2, pp. 505 – 514, 2006.

[113] T. Huppert, R. Hoge, A. Dale, M. Franceschini, and D. Boas, "Quantitative spatial comparison of diffuse opticl imaging with blood oxygen level-dependent and arterial spin labeling-based funtional magnetic resonance imaging," *Journal of Biomedical Optics*, vol. 11, no. 6, 2006. cited By (since 1996) 7.

[114] F. Irani, S. M. Platek, S. Bunce, A. C. Ruocco, and D. Chute, "Functional near infrared spectroscopy (fnirs): An emerging neuroimaging technology with important applications for the study of brain disorders.," *Clinical Neuropsychologist*, vol. 21, no. 1, pp. 9 – 37, 2007.

[115] H. Zhang, Y.-J. Zhang, C.-M. Lu, S.-Y. Ma, Y.-F. Zang, and C.-Z. Zhu, "Functional connectivity as revealed by independent component analysis of resting-state fnirs measurements," *NeuroImage*, vol. 51, no. 3, pp. 1150 – 1161, 2010.

[116] C. Hesse and C. James, "The fastica algorithm with spatial constraints," *Signal Processing Letters, IEEE*, vol. 12, pp. 792 – 795, nov. 2005.

[117] I. Schelkanova and V. Toronov, "Optimal quantitation of the cerebral hemodynamic response in functional near-infrared spectroscopy," *Opt. Express*, vol. 18, pp. 19386–19395, Aug 2010.

[118] N. C. et al, "Performance of blind source separation algorithms for fmri analysis using a group ica method," *Magnetic Resonance Imaging*, vol. 25, no. 5, pp. 684 – 694, 2007.

[119] J. D. Van Horn, J. S. Grethe, P. Kostelec, J. B. Woodward, J. A. Aslam, D. Rus, D. Rockmore, and M. S. Gazzaniga, "The functional magnetic resonance imaging data center (fmridc): the challenges and rewards of largescale databasing of neuroimaging studies," *Philosophical Transactions of the Royal Society of London. Series B: Biological Sciences*, vol. 356, no. 1412, pp. 1323–1339, 2001.

[120] W. Zijlstra, A. Buursma, and W. Meeuwsen-van der Roest, "Absorption spectra of human fetal and adult oxyhemoglobin, de- oxyhemoglobin, carboxyhemoglobin, and methemoglobin," *Clin Chem*, vol. 37, no. 9, pp. 1633–1638, 1991.